Gut distension evokes rapid neural dynamics in vagal and hindbrain populations of larval zebrafish

Minel Arinel[1*], John A. Atkinson[1], Karina M. Matos-Fernández[1], Evan P. Drage[1], Matt Hawkyard[2], Eva A. Naumann[1*]

[1]Department of Neurobiology, Duke University School of Medicine, Durham, NC, United States
[2]Aquaculture Research Institute, University of Maine, Orono, ME, United States

***Correspondence:**

Minel Arinel (minel.arinel@duke.edu)
Eva A. Naumann (eva.naumann@duke.edu)

Highlights:

- Zebrafish enteroendocrine cells regulate nutrient-specific feeding behaviors
- Left and right vagus similarly encode gut distension and nutrients
- Gut distension drives rapid, widespread neural responses across the hindbrain
- AITC uniquely evokes dynamics with slow onsets in vagal and hindbrain neurons

Summary

Animals sense food quantity and quality to regulate feeding behaviors essential for survival. Enteroendocrine cells (EECs) in the gut epithelium detect luminal distension and nutrients, signaling this information to the brain via vagal sensory neurons. However, how mechanosensory and chemosensory signals are dynamically encoded by gut-brain circuits remains unclear, particularly during early development. Leveraging the transparency and genetic tractability of larval zebrafish, we developed an assay using odorless, alginate-encapsulated particles designed to release nutrients after consumption. Using this approach, we demonstrated that larval EECs regulate nutrient-specific feeding. To determine how these post-ingestive signals are neurally encoded, we developed a microgavage method enabling simultaneous stimulus delivery to the gut and volumetric two-photon calcium imaging. We found that gut distension alone drove widespread activation and suppression in vagal ganglia and dorsal hindbrain, emerging as a dominant enteric signal in early development. Although nutrient-evoked responses shared temporal features with distension, allyl isothiocyanate (AITC)–an aversive compound found in wasabi–elicited distinct neural dynamics with slow onset. These findings reveal that fast gut-to-brain communication emerges early in life, with distension and aversive cues dynamically and differentially encoded in developing interoceptive circuits.

Keywords: gut-brain, zebrafish, enteroendocrine cell, feeding behavior, calcium imaging, distension, sensory encoding

Introduction

Animals need to rapidly detect the quantity and quality of ingested food to make adaptive feeding decisions essential for survival. While pre-ingestive cues such as taste and smell initiate feeding, the gut provides definitive confirmation of how much and what has been consumed[1,2]. This mechanosensory and chemosensory information is relayed to the brain to initiate digestion, prevent ingestion of harmful substances, and trigger satiety throughout adulthood[3–6]. Yet, how gut-brain communication unfolds during early development remains poorly understood[7,8].

In adults, gut-brain signaling is a well-established regulator of feeding behavior. Central to this signaling are sensory enteroendocrine cells (EECs), which comprise ~1% of the intestinal epithelium and detect luminal distension and nutrients[9–11]. EECs promote food intake during hunger, reduce intake after nutrient detection, and trigger aversive responses upon sensing harmful compounds[12–14].

A specialized subset of EECs, termed neuropods, forms synaptic connections with vagal sensory neurons that innervate the gut[1,2,11,12,15–21]. These vagal afferents rapidly transmit mechanosensory and chemosensory information to the brain via both EEC signaling and their intrinsic receptors[16,20,22–25]. In adult rodents, these afferents exhibit molecular[26], anatomical[6,27], and functional[6,27] lateralization between the left and right branches. Vagal neurons project to the nucleus tractus solitarius (NTS) and area postrema (AP) in the brainstem[6,28–30], which then relay this information to higher-order brain regions[6,20,31] and to the dorsal motor nucleus of the vagus[6,32,33], completing a bidirectional feedback loop to modulate peripheral physiology.

Despite growing insights into the molecular and anatomical organization of this system, the temporal encoding strategies used by gut-brain circuits remain poorly defined. Vagal sensory neurons can integrate mechanical and nutrient cues in a concentration-dependent manner[34] and show heterogeneous activity kinetics[35,36]. Similarly, neurons in the NTS can be activated or suppressed depending on the stimulated gastrointestinal organ and can display diverse response durations to gut distension[37]. However, most existing studies rely on anesthetized animals, limiting our understanding of dynamic gut-brain signaling in awake, developing organisms[38].

Larval zebrafish are a powerful model to investigate brain-body communication during early life. Unlike mammals, zebrafish develop externally, allowing direct observation and manipulation at early ages[39]. By 5 days post-fertilization (dpf), they have resorbed their yolk, developed a functional gut containing EECs, and initiated exogenous feeding[40,41]. Zebrafish share key molecular and anatomical features of the mammalian gut-brain axis, including molecularly defined EEC subtypes, vagal innervation of the gut, and homologous brainstem circuits[40–45]. Their transparency and small size enable optical access to both the gut and the brain, making them uniquely suited to dissect gut-brain signaling *in vivo*.

Previous studies in larval zebrafish have shown that EECs and vagal neurons express receptors for mechanical (e.g., Piezo2) and chemical (e.g., Sglt1, Glyt1, Trpa1) stimuli and exhibit stimulus-evoked responses[42,43,46–48]. EECs form basal projections toward vagal terminals resembling mammalian neuropods[42,43]. Vagal neurons are activated by intraluminal delivery of glucose[49] and the Trpa1 agonist allyl isothiocyanate (AITC)[43], a pungent compound found in wasabi, suggesting that gut-brain circuits are functionally active at larval stages. However, it remains unknown whether these signals influence feeding behavior and how they are rapidly and differentially encoded in the developing nervous system.

Here, we exposed hungry larval zebrafish to alginate-encapsulated particles that release nutrients after ingestion, thereby isolating gut-derived responses from exteroceptive cues. Using this assay, we show that EECs regulate nutrient-specific feeding behaviors, implicating gut-brain signaling in early feeding decisions. To investigate how these gut-derived signals are represented in the brain, we developed a prism-guided microgavage method compatible with two-photon calcium imaging in awake larvae. This approach enabled precise enteric stimulation while simultaneously recording neural activity in real time. We mapped stimulus-evoked activity across the bilateral vagal sensory ganglia and dorsal hindbrain,

including the vagal sensory lobe (homologous to NTS[50]), AP, and vagus motor nucleus (homologous to the dorsal motor nucleus of the vagus[51]). Our findings reveal that vagal neurons encode fast, dynamic information about gut distension with minimal lateralization. Compared to nutrient-evoked activity, distension emerged as a dominant driver of vagal and hindbrain responses in early development. In contrast, repeated stimulation with the aversive compound AITC triggered distinct temporal dynamics characterized by slow onsets. Together, these results establish larval zebrafish as a tractable model for investigating rapid gut-brain communication and demonstrate that distension and aversion are dynamically encoded in developing interoceptive circuits.

Results

Amino acids increase gut-mediated feeding

To determine how nutrient signaling from the gut regulates feeding, we encapsulated specific nutrients within complex particles[52,53] (CPs) that bypass exteroceptive chemosensing and restrict exposure to the gastrointestinal tract (**Figure 1A**). To form CPs, nutrients were combined with sodium fluorescein in an aqueous solution, encapsulated within liposomes, and embedded in an alginate matrix (**Figure 1B**). Upon ingestion, CPs expose their encapsulated nutrients to the gut epithelium, where EECs may detect and relay nutrient-specific signals to the brain.

Following 24 hours fasting, 9-dpf zebrafish were fed with CPs (0.05 mg/L, 25 mM nutrient concentration; **Figure 1C**). After 45 minutes of free feeding, zebrafish were euthanized, fixed, and embedded on their side to quantify particle consumption by measuring gut fluorescence (**Methods**).

We designed different CPs (**Figure 1D**), including empty particles containing only sodium fluorescein as negative controls (Ctrl; **Figure S1**). Sodium chloride (NaCl) particles acted as an additional negative control for potential olfactory detection through nutrient leaching, since zebrafish avoid NaCl via olfactory pathways[54,55]. For nutrients, we tested glucose (Glu), since it activates zebrafish EECs[42,43] and is highly rewarding in mammals[56–58]. Additionally, we generated CPs containing the amino acids glycine (Gly) and alanine (Ala) as they increase feeding across various fish species and are abundant in natural marine prey[59,60].

To quantify the consumption of different CPs, we measured total gut fluorescence in individual zebrafish (**Figures 1E** and **S1A**). Due to significant batch-to-batch variation with Ctrl particles (**Figure S1B**), we normalized each fish's fluorescence value to its respective median batch Ctrl intensity. As expected, NaCl particles did not change feeding relative to Ctrl, confirming that consumption is not affected by nutrient leaching. Compared to the Ctrl group, zebrafish exposed to glycine or alanine, but interestingly not glucose, significantly increased consumption (**Figure 1F**). These results demonstrate that exposure of glycine and alanine to the gut promotes feeding, underscoring the ecological importance of amino acids in the zebrafish diet.

EEC depletion alters food approach and nutrient-specific feeding

To test whether gut-mediated feeding behaviors are modulated by EECs, we chemogenetically depleted EECs from the proximal and midgut using diphtheria toxin[43] (EEC^{DTA}; **Figure 1G**) and exposed EEC^{DTA} zebrafish to the same CPs as wild-type (WT) cohorts. Examining whether EEC depletion altered the likelihood of food approach, we quantified the percentage of zebrafish containing any fluorescent particles in their gut. EEC^{DTA} batches had significantly lower and more variable food approach compared to WT across stimuli (**Figure 1H**). However, in EEC^{DTA} zebrafish, glucose, glycine, and alanine each significantly increased consumption compared to Ctrl, whereas NaCl did not (**Figure 1I**). Notably, the relative intensities of nutrients were greater in EEC^{DTA} zebrafish compared to WT (glucose: ~1.8x, glycine: ~3.2x, alanine: ~4.7x). To determine whether this increased fluorescence in EEC^{DTA} fish was caused by impaired

peristalsis, we compared gut motility between unfed and fed EEC^{DTA} zebrafish relative to WT and Cre-negative controls (**Figure S2**; **Video S1**). As expected, fed zebrafish exhibited significantly higher gut motility compared to unfed fish, but no differences in gut motility were detected across genotypes. These results, together with the nutrient-specific increase in fluorescence in EEC^{DTA} fish, suggest that the elevated fluorescence reflects greater nutrient intake rather than impaired gut clearance. Collectively, these findings reveal a dual role for EECs in modulating feeding behavior. While EEC depletion reduced the likelihood of initiating feeding, it enhanced nutrient intake once feeding began. These results suggest that even in early development, zebrafish EECs regulate nutrient-specific feeding by conveying satiety-related signals to the brain.

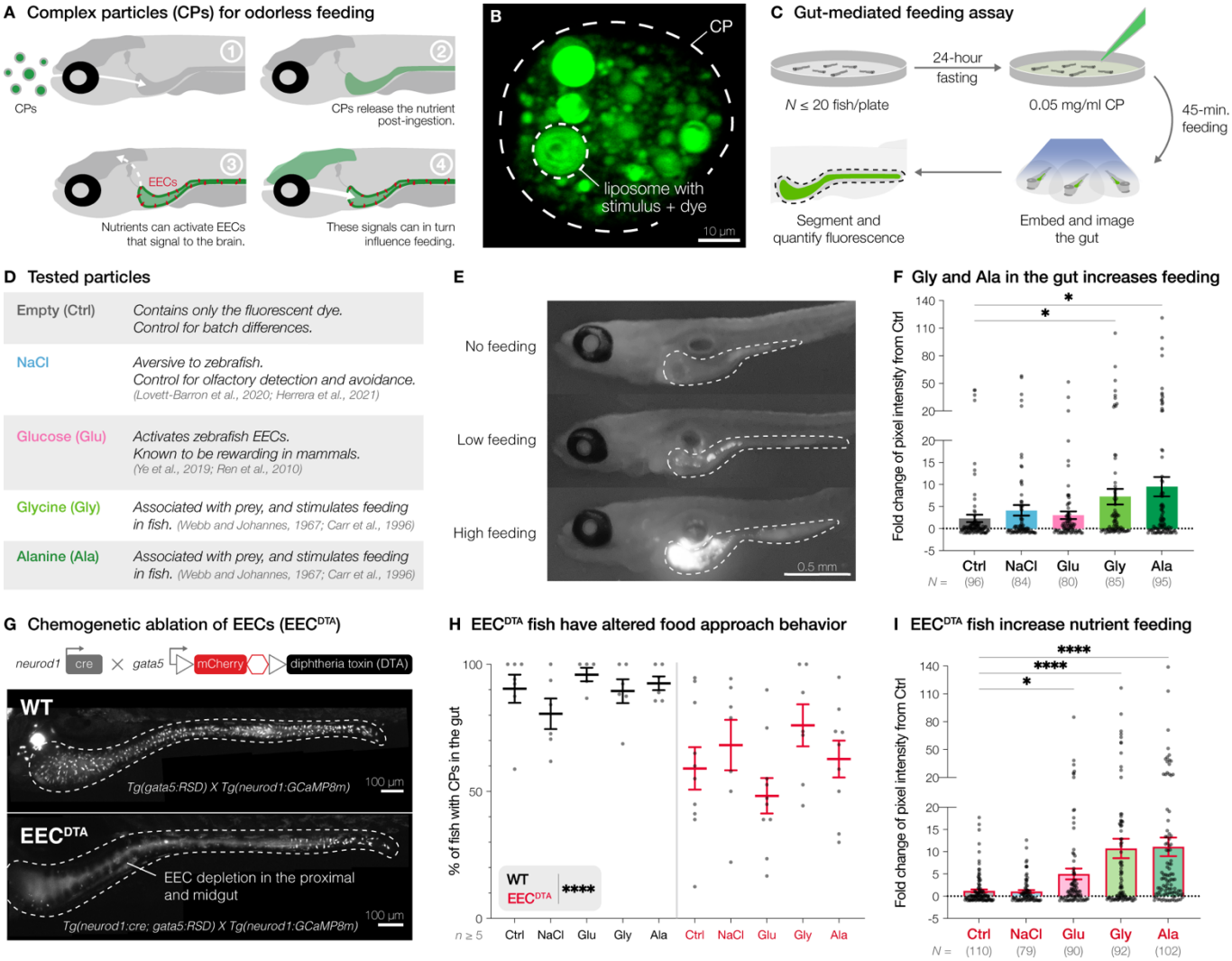

Figure 1 | Zebrafish EECs mediate nutrient-specific feeding

(**A**) Schematic illustrating gut nutrient delivery by feeding complex particles (CPs), which bypass exteroceptive chemosensation as they expose their contents only in the gut, potentially activating EECs (red).
(**B**) Two-photon image of a CP with fluorescent liposomes surrounded by alginate matrix (dashed outline).
(**C**) After 24 hours of fasting, freely swimming zebrafish were exposed to CPs loaded with different nutrients. After 45 minutes of feeding, zebrafish were fixed to quantify gut fluorescence.
(**D**) Table of tested nutrients and rationale for selection.

(**E**) Side views of representative zebrafish with no, low, and high consumption of fluorescent CPs in the gut (dashed outlines).
(**F**) Gut fluorescence in wild-type (WT) zebrafish, plotted as fold change from the median fluorescence of the batch control. Compared to empty CPs (Ctrl, $N = 96$) CPs with glycine (Gly, $N = 85$, $^{*}P = 0.0155$) and alanine (Ala, $N = 95$, $^{*}P = 0.0119$) drove significant increase in feeding, unlike NaCl ($N = 84$, $P > 0.9999$) or glucose (Glu, $N = 80$, $P = 0.7261$, Kruskal-Wallis and Dunn's multiple comparisons tests). Dots represent individual fish.
(**G**) Top: schematic of chemogenetic EEC ablation. Bottom: representative gut images of Cre-negative and Cre-positive EEC-depleted fish (EEC^{DTA}).
(**H**) Percentage of fish with any gut fluorescence in each batch of WT and EEC^{DTA} zebrafish across stimuli ($n \geq 5$ plates). EEC^{DTA} exhibited significantly lower % of fish with CPs ($^{****}P < 0.0001$, Kolmogorov-Smirnov test) with higher variability ($^{****}P < 0.0001$, Fligner-Killeen test) than WT. Dots represent experimental batches.
(**I**) Gut fluorescence in EEC^{DTA} zebrafish fed with CPs, plotted as fold change from the median fluorescence of the batch control. Compared to empty CPs ($N = 110$), EEC^{DTA} zebrafish ate significantly more CPs filled with glucose ($N = 90$, $^{*}P = 0.0163$), glycine ($N = 92$, $^{****}P < 0.0001$), and alanine ($N = 102$, $^{****}P < 0.0001$), but not with NaCl ($N = 79$, $P > 0.9999$, Kruskal-Wallis and Dunn's multiple comparisons tests).
Dots represent individual fish (F and I). Mean ± SEM.

Microgavage during neural recording of gut-brain signaling

To investigate how these enteric signals are encoded by the nervous system, we next aimed to record gut-derived neural responses, focusing on signals transmitted via the vagus nerve to the hindbrain. Intriguingly, larval zebrafish EECs exhibit basal protrusions morphologically resembling neuropods that form synapses in mammals[43] (**Figure 2A**). However, not much is known about rapid gut-brain communication at this developmental stage, as recordings are challenging in mammals during development[61,62].

Building on a previous method[63] for microgavaging anesthetized larval zebrafish, we developed a novel microgavage technique to deliver nanoliters of stimuli into the gut during simultaneous two-photon calcium imaging in awake larval zebrafish (**Figures 2B** and **S3**). To eliminate the need for anesthesia, we designed a flexible microgavage needle from aluminosilicate glass with an extended taper and a fine tip (≤20 µm outer diameter; **Figure S3C**), allowing gentle insertion through the pharynx and esophagus without breakage. A ~30° bend near the tip enabled precise alignment with the gastrointestinal tract, ensuring accurate stimulus delivery and an optimal imaging angle. Lastly, we placed a prism next to the fish for simultaneous visualization from ventral and lateral perspectives within a single field of view (**Figures 2C, S3A,** and **S3B**).

To perform microgavage during two-photon calcium imaging, we embedded 6–10 dpf *Tg(elavl3:H2B-GCaMP8m)* zebrafish, which express the nuclear-localized calcium indicator GCaMP8m, in 1.5% low-melting-point agarose. Two imaging configurations were optimized to record neural activity in either vagal ganglia or dorsal hindbrain (**Figures 2D, S3A,** and **S3B**). As the microgavage needle is guided through the gastrointestinal tract, we monitored for any signs of discomfort or pain, such as twitching, via infrared camera (**Video S2**). After each experiment, we confirmed stimulus localization in the gut and verified that the procedure did not cause injury (**Figure 2E**).

To validate that neural responses were driven by gut stimulation rather than the microgavage procedure, we compared neural activity prior to needle insertion, post-insertion without stimulus injection, and after intraduodenal stimulus delivery (**Figure 2F**). We confirmed that neuronal activity was stimulus-dependent and time-locked to gut stimulus delivery. Therefore, our microgavage method provides the necessary temporal and spatial precision to reliably capture fast gut-derived neural signals, confirming functional gut-to-brain connectivity in larval zebrafish.

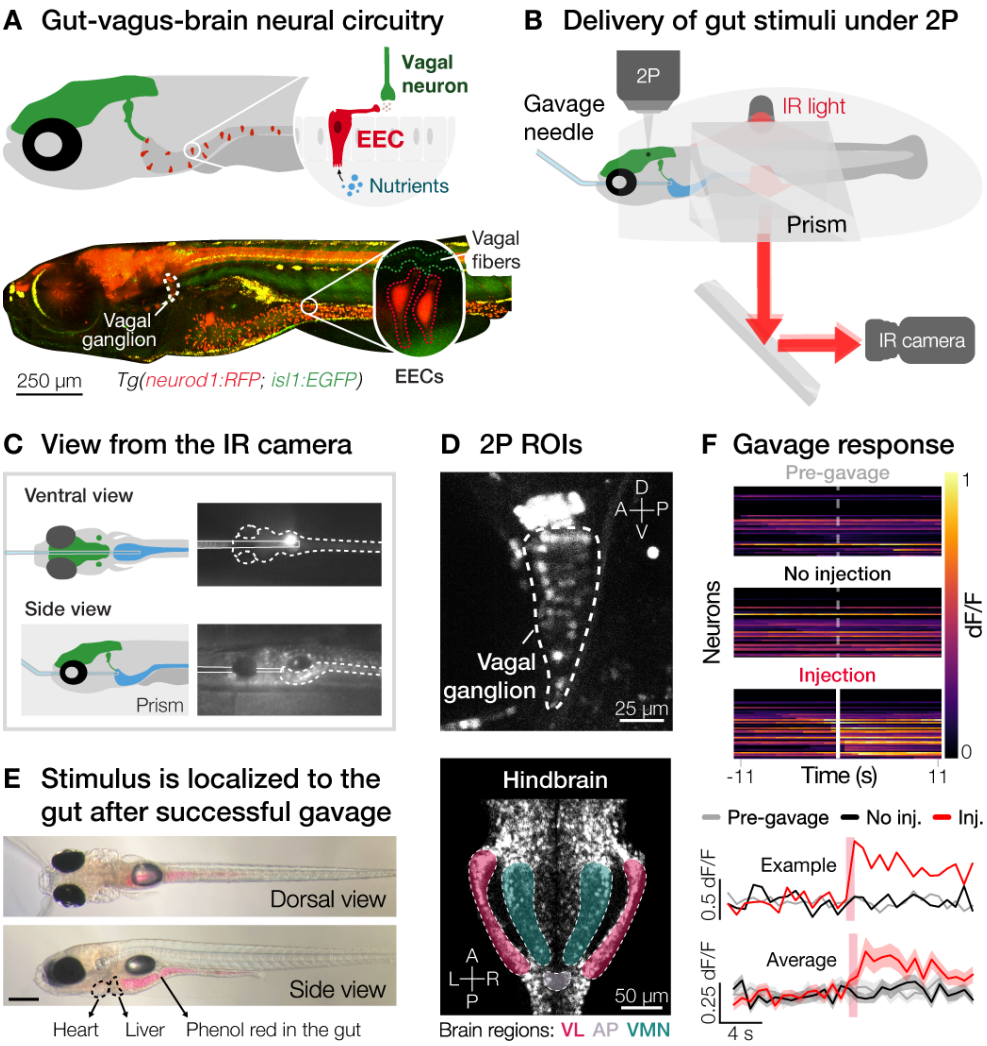

Figure 2 | Microgavage during two-photon imaging to record gut-mediated neural activity

(**A**) Top: schematic of the gut-vagus-brain neural circuitry. Bottom: two-photon image of a 7 dpf *Tg(neurod1:RFP; isl1:EGFP)* zebrafish, showing the entire EEC population (red) and vagal neurons (green), with a zoom-in of two EECs with protrusions toward vagal fibers.
(**B**) Schematic of the microgavage setup with zebrafish embedded in agarose for imaging. A bent gavage needle is guided into the gut using a prism mirror for simultaneous ventral and side visualization, ensuring precision enteric stimulus delivery.
(**C**) Left: cartoons of the infrared (IR) camera's field of view. Right: snapshots of ventral and side views for precise microgavage needle positioning.
(**D**) Two-photon image of the left vagal ganglion (top). Scale bar = 25 µm. A, anterior; P, posterior; D, dorsal; V, ventral. In the hindbrain (bottom), the vagal sensory lobes (VL), area postrema (AP, located more dorsally than the shown plane), and vagus motor nucleus (VMN) can be imaged simultaneously. Scale bar = 50 µm.
(**E**) Transmission images after successful microgavage show enteric stimulus localization exclusively in the gut (red), confirming intact internal organ morphology (e.g., heart and liver). Scale bar = 250 µm.
(**F**) Vagal neurons show time-locked responses specifically to enteric stimulation, not to the microgavage procedure. Top: heatmaps of neural dynamics before microgavage, after needle insertion (dashed lines) without injection, and during enteric stimulus injection (white line). Bottom: dF/F traces of a representative neuron and average population response shown in the heatmaps above.
Red vertical lines indicate time of injection. Mean ± SEM.

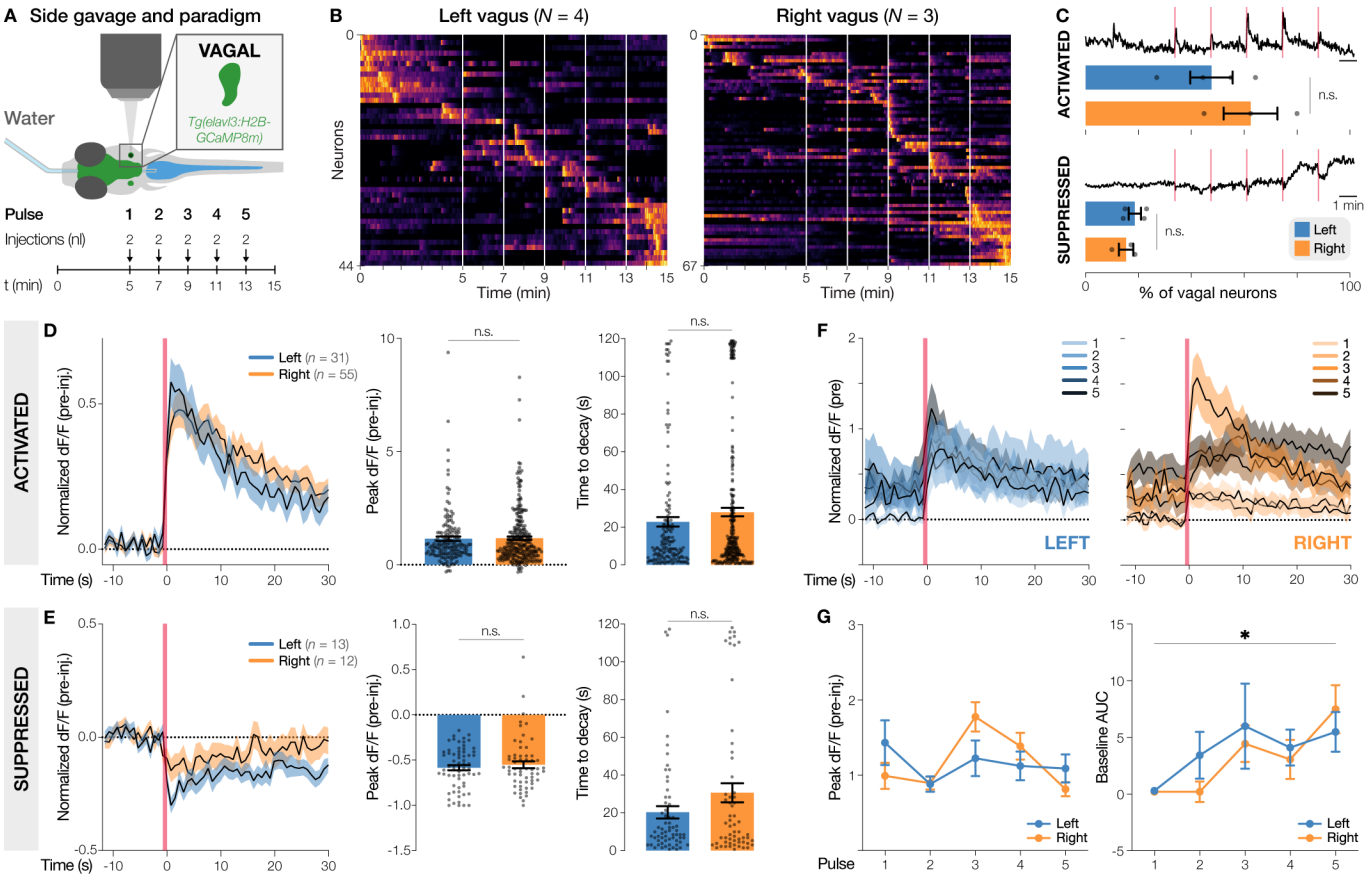

Figure 3 | Gut distension elicits bilateral activation and suppression of vagal neurons

(**A**) Experimental setup. 6–10 dpf *Tg(elavl3:H2B-GCaMP8m)* zebrafish were embedded on their side and gavaged with E3 medium ("water"), delivering five pulses of 2 nL.
(**B**) Heatmaps of all responsive neurons from left (N = 4 fish) and right (N = 3 fish) vagal ganglia sorted by peak time. White lines indicate injection times.
(**C**) Representative normalized dF/F traces and percentages of activated (top) or suppressed (bottom) vagal neurons, which were similar between left and right vagus (activated: P = 0.2981, suppressed: P = 0.3941, unpaired t-tests). Dots represent individual fish.
(**D**) Temporal dynamics of activated neurons around injections. Left: average dF/F traces from left (blue, n = 31 neurons) and right (orange, n = 55 neurons) vagus, normalized to the pre-injection baseline. Right: peak dF/Fs (normalized to pre-injection baseline) and times to decay showed no significant lateralization (peak dF/F: P = 0.6491, Mann-Whitney test, time to decay: P = 0.5479, Kolmogorov-Smirnov test). Dots represent individual traces.
(**E**) Temporal dynamics of suppressed neurons. Left (n = 13 neurons) and right (n = 12 neurons) vagal neurons did not differ significantly in peak dF/F (P = 0.9001, Mann-Whitney test) or time to decay (P = 0.7082, Kolmogorov-Smirnov test). Dots represent individual traces.
(**F**) Average dF/F of activated neurons for pulse 1-5 (light to dark), normalized to the baseline before the first pulse.
(**G**) Peak dF/F (normalized to pre-injection baseline) shows no significant lateralization. dF/F area under the curve (AUC) of activated neurons significantly increased with higher distension (*P = 0.0239, mixed-effects analysis and Friedman test).
Injection times are marked by red lines (C–F). n.s., not significant. Mean ± SEM.

Vagal afferents bilaterally encode gut distension

Since each microgavage injection inherently induces gut distension, we first investigated vagal responses to stretch stimuli without the presence of nutrients. Recording neural activity in either the left or right vagus, we injected the standard E3 medium in which zebrafish are raised (**Methods**), hereafter referred to as "water", directly into the gut lumen in five pulses of 2 nL, each separated by a 2-minute interval (**Figure 3A**).

Extracting dF/F traces of all vagal neurons, we identified those with stimulus-locked activity (**Figures 3B**, **S4A, and S5A**; **Video S3**). Notably, we observed not only neurons activated by gut distension, but also neurons exhibiting suppression (**Figure 3C**). The proportions of activated and suppressed neurons did not differ between left and right vagal ganglia (**Figure 3C**). Similarly, average temporal dynamics of responses to gut distension were comparable between left and right vagal neurons (**Figures 3D** and **3E**), suggesting symmetric encoding of gut mechanosensation.

To evaluate how neuronal responses evolve with increasing gut distension, we examined temporal dynamics across consecutive gavage pulses (**Figures 3F**, **3G**, **S5B**, and **S5C**). In both left and right vagal ganglia, activated neurons exhibited progressively elevated baseline fluorescence as distension increased. However, changes in peak amplitudes remained unchanged (**Figure 3G**). As population-level analyses can obscure neuron-specific dynamics, we further classified neurons based on their overall peaks across pulses as "integrating" or "habituating" (**Figure S4E**). Only a small proportion of neurons showed integration (left: 7%, right: 10%) or habituation (left: 2.5%, right: 2.3%), with no significant differences between ganglia (**Figure S5D**). This suggests that vagal afferents encode distension predominantly in a monotonic manner, with minimal lateralization between the left and right vagus. These findings support the idea that vagal circuits function as early detectors of distension intensity and reveal that, unlike the lateralized vagal responses observed in mammals, larval zebrafish encode gut distension symmetrically.

Gut distension broadly activates dorsal hindbrain circuits

We next performed volumetric calcium imaging in the dorsal hindbrain to investigate how mechanosensory signals are propagated to downstream brain regions (**Figure 4A**). We observed widespread distension-evoked activation and suppression in multiple interoceptive regions, including the vagal sensory lobe (VL), area postrema (AP), and vagus motor nucleus (VMN; **Figures 4B–4D**). The lack of anatomical organization indicates that distension signals are broadly encoded across the dorsal hindbrain (**Figures 4C** and **S6**). The proportions of activated and suppressed hindbrain neurons were comparable to those in vagal ganglia (**Figure 4D**), suggesting a conservation of stretch responsiveness from the vagus to hindbrain.

The average temporal dynamics of activated neurons were broadly conserved across vagal and hindbrain regions (**Figure 4E**). Suppressed neurons also displayed similar response profiles, except for AP neurons, which exhibited significantly weaker suppression compared to vagal neurons (**Figure 4F**). To examine hindbrain responses to increasing gut distension, we compared neural activity across sequential pulses (**Figure 4G**). VMN neurons showed progressively smaller peaks with higher distension intensities, suggesting adaptation (**Figure 4H**). Notably, baseline fluorescence increased over repeated pulses in the VL, VMN, and inferior dorsal medulla oblongata (Inf), mirroring trends observed in vagal neurons (**Figure 4H**). These results indicate that while immediate responses in motor regions diminish with increasing distension, baseline activity steadily rises in both sensory and motor areas. This broad and fast encoding across the dorsal hindbrain highlights gut distension as a salient interoceptive signal in larval zebrafish.

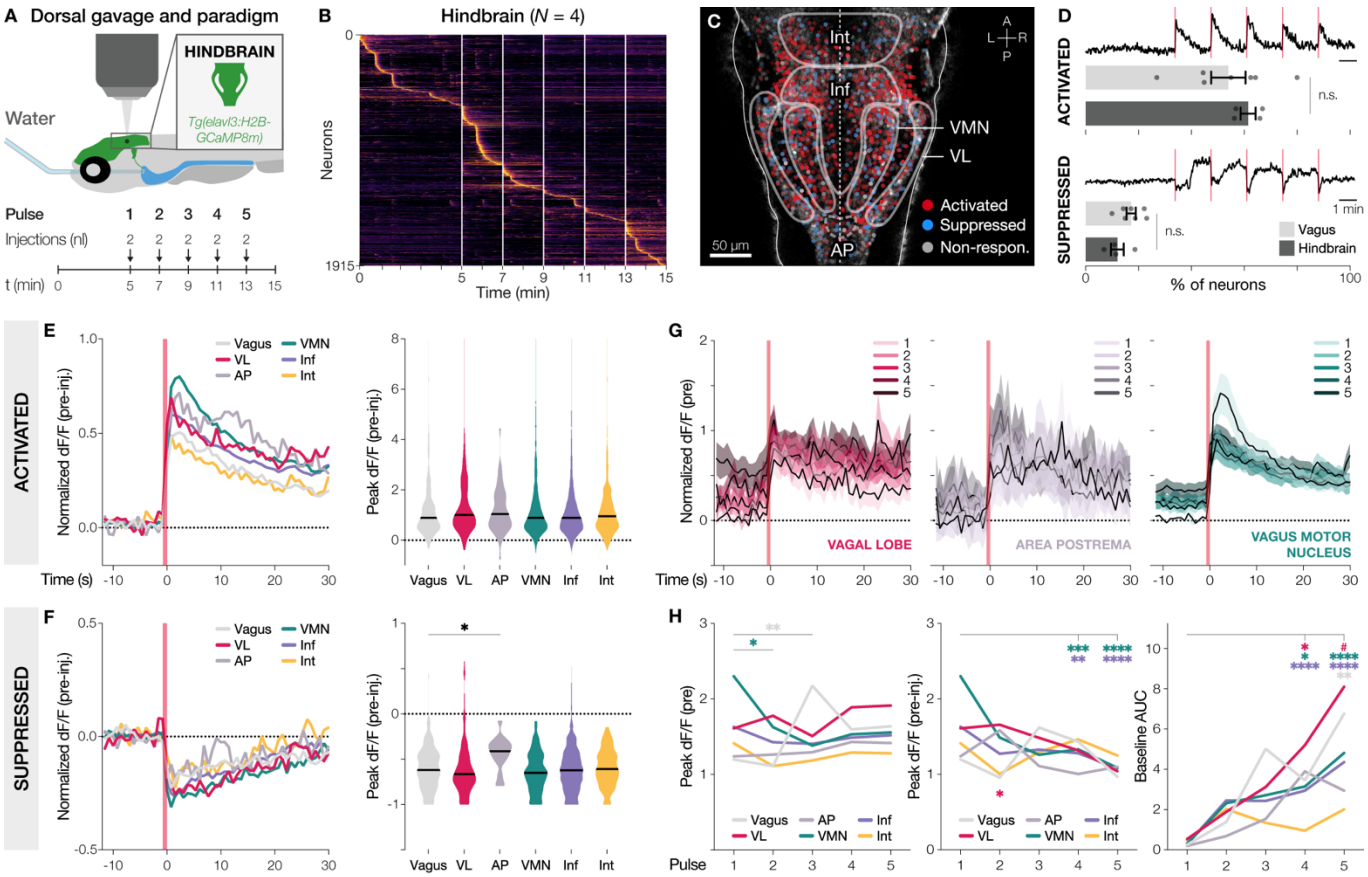

Figure 4 | Gut distension evokes widespread neuronal activity across the dorsal hindbrain

(**A**) For hindbrain distension recordings, *Tg(elavl3:H2B-GCaMP8m)* zebrafish were embedded dorsal-side-up and gavaged with water, five pulses of 2 nL.
(**B**) Heatmap of all responsive neurons across the dorsal hindbrain sorted by peak time (N = 4 fish). White lines indicate injection times.
(**C**) Spatial distribution of hindbrain neurons classified as activated (red), suppressed (blue), or non-responsive (gray), plotted on reference hindbrain. Dot opaqueness indicates higher average peak dF/F (pre-inj.) across pulses. Area postrema (AP, dashed line) lies dorsally out of the depicted plane. A: anterior, L: left, P: posterior, R: right.
(**D**) Representative normalized dF/F traces and percentages of activated (top) or suppressed (bottom) neurons, which were similar between the vagus and hindbrain (activated: P = 0.4259, suppressed: P = 0.1106, unpaired t-tests). Dots represent individual fish.
(**E**) Temporal dynamics of activated neurons around injections. Left: average dF/F traces from vagus (light gray, n = 86 neurons), vagal sensory lobe (VL, pink, n = 55 neurons), area postrema (gray, n = 8 neurons), vagus motor nucleus (VMN, green, n = 291 neurons), inferior dorsal medulla oblongata (Inf, purple, n = 879 neurons), and intermediate dorsal medulla oblongata (Int, yellow, n = 95 neurons). Right: peak dF/Fs (pre-inj.) across regions were not significantly different (P = 0.1139, Kruskal-Wallis test).
(**F**) Temporal dynamics of suppressed neurons. Left: average dF/F traces from vagus (n = 25 neurons), VL (n = 21 neurons), AP (n = 3 neurons), VMN (n = 46 neurons), Inf (n = 186 neurons), and Int (n = 25 neurons). Right: AP neurons showed less suppression compared to vagal neurons (*P = 0.0463, Kruskal-Wallis and Dunn's multiple comparisons tests).
(**G**) Average dF/F traces of activated neurons for pulse 1-5 (light to dark), normalized to the baseline of the first pulse.
(**H**) Peak dF/Fs (pre), peak dF/Fs (pre-inj.), and baseline AUCs of activated neurons across pulses. Peak dF/F (pre-inj.): VMN and Inf neurons had smaller changes in peak with increasing distension (P < 0.005). Baseline

AUC: Vagal, VL, VMN, and Inf neurons exhibited increased baseline activity with increasing distension ($P < 0.03$, VL pulse 1 vs. 5: $^{\#}P = 0.0507$, mixed-effects analyses with Šídák's multiple comparisons).
Injection times are marked by red lines. $^{*}P < 0.05$, $^{**}P < 0.01$, $^{***}P < 0.001$, $^{****}P < 0.0001$. n.s., not significant.
Line and bar graphs show mean ± SEM. Violin plots show median.

Neuronal response subtypes to increasing gut distension

To characterize heterogeneous neural responses across repeated pulses, we categorized activated and suppressed neurons as "monotonic", "integrating", or "habituating" based on their peak amplitudes (**Figure S7A**). Among these, activated & monotonic (aM), suppressed & monotonic (sM), and activated & integrating (aI) subtypes were consistently observed across both the vagus and hindbrain in all fish (**Figures S7B** and **S7C**). The proportions of these subtypes did not differ significantly across regions (**Figure S7D**), and subtypes were not spatially clustered (**Figure S8**), suggesting broad recruitment rather than regional specialization for response dynamics to distension.

We next characterized the temporal profiles of each subtype across regions (**Figure S9**). While monotonic neurons were defined by the absence of significant trends in peak dF/Fs, aM neurons in the VMN showed diminishing peaks and shorter decay times over successive pulses, resembling habituation-like dynamics (**Figures S9A** and **S9B**). In contrast, aI neurons exhibited consistent amplification of peaks across pulses in all regions, reflecting progressive integration of mechanosensory input (**Figures S9E** and **S9F**). Interestingly, baseline fluorescence rose across all subtypes in the VMN and Inf, potentially reflecting global increases in neural activity driven by slow hormonal feedback (**Figure S9**). Together, these findings reveal diverse and distributed spatiotemporal coding strategies for encoding enteric distension signals across vagal and hindbrain circuits in early development.

Chemosensory encoding of AITC features slow-onset dynamics

To examine how additional chemosensory information influences gut-brain signaling, we injected nutrient solutions at the same concentration as in the CPs of feeding experiments (25 mM; **Figure 1**). Based on findings from our gut-mediated feeding assay and previous literature[43,64] (**Figure 1F**), we selected glucose as a neutral, glycine as an appetitive, and AITC as an aversive chemical stimulus (**Figure 5A**). As with distension, we observed no strong lateralization between the left and right vagus across stimuli (**Figure S10**). Given the overall symmetry of responses, data from both ganglia were combined for subsequent analyses.

We then assessed how chemosensory signals were encoded across the dorsal hindbrain (**Figures 5C, S11A, and S11B**). Similar proportions of activated and suppressed neurons were observed between the vagus and hindbrain and across stimuli (**Figures 5D and S11C**). However, spatial analyses revealed stimulus-specific topographies in the hindbrain, with more anteriorly distributed glycine-responsive neurons and more posterior AITC-responsive neurons (**Figure S12A**). This separation was significantly more pronounced in the VL, where glycine- and AITC-responsive neurons showed the greatest spatial divergence (**Figure S12B**). Average temporal dynamics revealed that AITC evoked significantly slower activation in VL, VMN, and Inf neurons (**Figures S11D and S11E**). Suppressed neurons in the VL also showed slower onset to AITC compared to both water and glucose (**Figures S11F and S11G**). These results suggest that AITC drives distinct temporal activity within the vagus-hindbrain circuit, supporting the notion that the brain differentially encodes gut-derived aversive signals through stimulus-specific temporal dynamics.

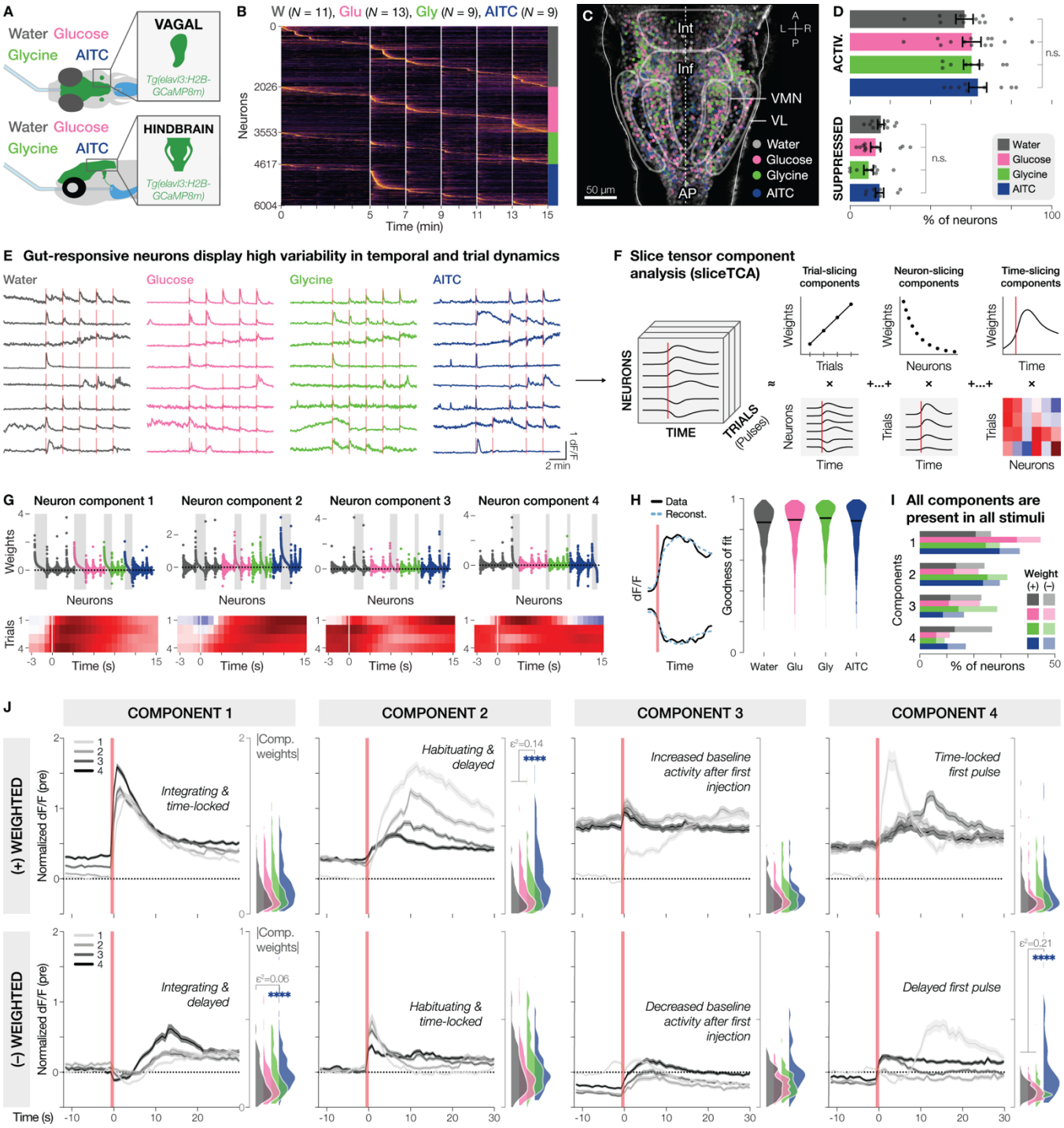

Figure 5 | Enteric stimuli drive complex temporal dynamics in vagal and hindbrain neurons

(**A**) Schematic of imaging configurations to record gut-evoked neural activity in vagal and hindbrain neurons in response to microgavage of water, glucose (25 mM), glycine (25 mM), or AITC (25 mM).
(**B**) Heatmap of all responsive vagal and hindbrain neurons sorted by peak time (water: *N* = 11 fish, gray, glucose: *N* = 13 fish, pink, glycine: *N* = 9 fish, green, AITC: *N* = 9 fish, blue). White lines indicate injection times.
(**C**) Spatial distribution of gut-responsive hindbrain neurons colored by stimulus identity. Dot opaqueness indicates higher average pulse peak dF/F (pre-inj.). Brain regions as in Figure 4C. A: anterior, L: left, P: posterior, R: right.

(**D**) Percentages of activated (top) or suppressed (bottom) neurons were not significantly different (n.s.) across stimuli (activated: $P = 0.7819$, one-way ANOVA, suppressed: $P = 0.1747$, Kruskal-Wallis test). Dots represent individual fish.
(**E**) Representative normalized dF/F traces for all enteric stimuli showing temporal and trial variability.
(**F**) Schematic of slice tensor component analysis (sliceTCA). Traces from all stimuli and regions were compiled into a 3D data tensor (trials x neurons x time). The first four successful trials were used for consistency. SliceTCA decomposes this tensor into trial-, neuron-, and time-slicing components, where the data tensor is approximated as the outer product of each component's weights and slice.
(**G**) Neuron-slicing components of the sliceTCA model. Weights are colored by stimulus. Neurons were clustered into the component with their highest weight (gray bars). Note that neurons may have positive or negative weights for their assigned component. White lines indicate injections.
(**H**) Left: representative trace reconstructions (blue dashed line) overlaid on raw data (black). Right: reconstruction goodness of fit per neuron, grouped by stimulus. Black lines show median.
(**I**) All enteric stimuli drove all four temporal neural dynamics, illustrated by the percentage of positive (darker) and negative (lighter) weighted clusters per stimulus, averaged across fish without significant differences across stimuli (mixed-effects analysis and Šídák's multiple comparisons test).
(**J**) Left: average dF/F traces of positive- and negative-weighted neurons per component, plotted across pulses (light to dark), increasing gut distension. Right: Stacked violin plots show absolute component weights per stimulus. Clusters C1–, C2+, and C4– had significantly stronger weights in AITC-responsive neurons, indicating AITC evokes diverse delayed dynamics. Other clusters had no significant differences across nutrients, reflecting the importance of distension-related dynamics. Only comparisons with $P < 0.05$ (Kruskal-Wallis and Dunn's multiple comparisons tests) and at least medium effect sizes ($\varepsilon^2 \geq 0.06$ with epsilon-squared and $|\delta| \geq 0.33$ with Cliff's delta) were considered significant.
Injection times are marked by red lines (D, E, and I). ****$P < 0.0001$. n.s., not significant. Mean ± SEM.

Enteric information is encoded in diverse temporal dynamics

To further dissect the neural dynamics evoked by repeated gut stimulation, we analyzed temporal patterns across pulses for all responsive vagal and hindbrain neurons (**Figure 5E**). Prompted by the heterogeneity in neuronal responses across time and injection pulses, we employed the unsupervised dimensionality reduction method slice tensor component analysis[65] (sliceTCA; **Figure 5F**). SliceTCA decomposes a three-dimensional data tensor, which is comprised of the injection pulses, neurons, and time, into separate components along each dimension, thus enabling a biologically interpretable representation of diverse response patterns.

An optimized parameter search that balanced cross-validation loss, reconstruction performance, and neuron-weight sparsity yielded a model with 0 trial-slicing, 4 neuron-slicing, and 1 time-slicing component (**Figures 5G, 5H, and S13**). Each of the four neuron-slicing components (C1–4) revealed pairs of distinct temporal dynamics, resulting in eight total neuron clusters. We assigned each neuron to one of these eight clusters based on its sign (positive (+) or negative (–)) and magnitude of its strongest neuron-slicing component weight. These clusters were similarly represented across the left and right vagus, brain regions, and nutrient stimuli (**Figure 5I**; **Table S2**), indicating the anatomically widespread recruitment of these temporal motifs, regardless of stimulus type or brain region.

Temporal analysis of component dynamics revealed distinct biological response signatures. While C1 captured integrating neurons across increasing gut distension (water: 26.46%, glucose: 44.85%, glycine: 29.73%, AITC: 37.05%), C2 clustered habituating neurons (water: 23.82%, glucose: 21.71%, glycine: 32.33%, AITC: 29.47%). Interestingly, C3 and C4 reflected unique dynamics associated with the onset of sensory input. C3 was defined by changes in baseline fluorescence after the first injection (water: 22.92%, glucose: 22.39%, glycine: 28.78%, AITC: 16.48%), whereas C4 characterized neurons that responded strongly to the initial pulse (water: 26.80%, glucose: 11.05%, glycine: 9.16%, AITC: 17.00%) (**Figures 5J and S14**). While components C1 and C2 dynamically encoded the ongoing state of gut

content, components C3 and C4 represented the initial sensory detection, likely signaling confirmation of consumption.

Finally, we assessed the contributions of each stimulus-responsive neuron to individual clusters. Most clusters exhibited comparable component weights across all stimuli, reinforcing that gut distension is the dominant visceral cue, even in the presence of nutrients that shape neural activity. However, three clusters (i.e., C1–, C2+, and C4–) displayed significantly higher weights from AITC-responsive neurons (**Figure 5J**). All three clusters exhibited slow response onsets, indicating that AITC consistently drives slower activation patterns. These findings demonstrate that while gut distension initiates robust neural responses with fast onsets, AITC drives temporally distinct, slow-onset populations across the vagus and hindbrain.

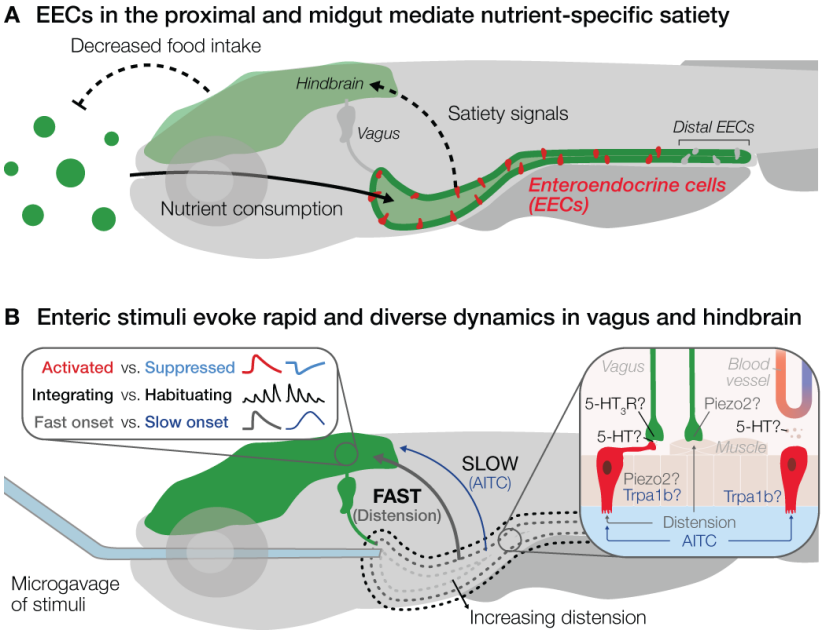

Figure 6 | Overview of behavioral and neural responses to enteric stimuli in larval zebrafish

(**A**) Cartoon illustrating the role of EECs in the proximal and midgut in regulating food approach and post-ingestive feeding. Upon nutrient consumption, like glucose or glycine, EECs communicate satiety signals that act on the brain to decrease food intake.
(**B**) Enteric stimuli evoke diverse temporal dynamics in vagal and hindbrain neurons. While gut distension is encoded with fast, time-locked neural signatures, the aversive compound allyl isothiocyanate (AITC) induces responses with slower onsets. While distension may activate Piezo2 channels on neuropod-forming EECs and/or Piezo2-positive vagal afferents that innervate the gut musculature, AITC activates Trpa1b on EECs[43], which may signal enteric information synaptically and/or hormonally. Both Piezo2 and Trpa1b are expressed in serotonin-producing enterochromaffin cells, suggesting that serotonin signaling via 5-HT_3 receptors on vagal neurons may contribute to gut-brain communication.

Discussion

Understanding how post-ingestive signals from the gut are communicated to the brain is critical for identifying the neural basis of feeding behaviors. By measuring the consumption of complex particles that bypass exteroceptive chemical signaling, we uncovered that EECs regulate feeding behaviors in early development. Using our novel microgavage method to deliver enteric stimuli during calcium imaging, we

demonstrate that fast gut-brain communication is present as soon as the gut functionally develops. Specifically, we demonstrate that zebrafish vagal afferents and their target neurons in the hindbrain encode diverse enteric signals, exhibiting rich temporal dynamics of activation and suppression related to feeding status and history. These results extend our understanding of interoceptive signaling, revealing that gut-derived mechanical and chemical stimuli modulate brain activity within seconds of ingestion, even in the developing vertebrate brain (**Figure 6A**).

To investigate whether and how enteric signaling contributes to feeding in larval zebrafish, we developed a gut-mediated feeding assay using CPs, which are commonly used in aquaculture to enhance nutrient retention in marine feeds[52,5352,53]. This approach enabled us to isolate the gut-mediated post-ingestive effects of appetitive and aversive nutrients on feeding. Glycine and alanine, amino acids abundant in the zebrafish's natural diet[60,66–68], robustly promoted feeding. In contrast, glucose, which drives consumption in mammals[69], had no such effect in fish. This nutrient-specific behavioral preference aligns with ecological observations, as zebrafish prey contains high levels of glycine, potentially serving as a chemical cue for foraging[59,60,70]. Additionally, the zebrafish homologue of the mammalian sweet taste receptor is more responsive to amino acids than sugars[71], reinforcing the relevance of amino acids in zebrafish feeding.

By comparing feeding in wild-type and zebrafish with depleted EECs[43], we uncovered a dual role for EECs promoting food approach, yet regulating consumption of nutrients once feeding was initiated. This dichotomy suggests a functional division among EEC subtypes. Some, such as ghrelin-expressing EECs, likely promote hunger and food approach[72–74], while others release satiety peptides, like cholecystokinin and peptide YY, to limit intake once nutrients are ingested[5,12,4274–76]. Removing these regulatory EECs may thus disrupt the balance between motivation to feed and satiation, resulting in increased intake after feeding has occurred. These findings highlight the multifaceted roles of EECs in shaping both anticipatory and post-consummatory aspects of feeding behavior shortly after the onset of exogenous feeding[40,41].

To begin dissecting how post-consummatory gut signals are relayed to the brain, we next developed a novel microgavage[63] method to deliver specific nutrients into the gut lumen while simultaneously recording neural activity in the brain at single-cell resolution. Importantly, this approach allows us to mimic naturalistic feeding by activating both mechanosensory and chemosensory signaling in awake zebrafish. In less than a second after enteric stimulus delivery, we observed widespread activation and suppression across vagal and hindbrain neurons. Our results revealed rapid gut-brain communication as early as 6 dpf, soon after the formation of a functional gut, suggesting the presence of fast synaptic mechanisms in early development[1,77].

Since the gut inherently distends during nutritive stimulus delivery, we first focused on mechanosensory signals. A key candidate for mediating distension detection is the mechanosensitive ion channel Piezo2, which has been implicated in sensing distension in peripheral organs, including the gastrointestinal tract[78–80], and is conserved from mammals to fish[81–83]. Notably, both EECs and vagal afferents express Piezo2[46,47], suggesting that mechanical signals may be sensed in multiple sensors along the gut-brain circuit[80,84,85] (**Figure 6B**). In EECs, Piezo2 is enriched in enterochromaffin cells and can initiate serotonin release in response to distension, modulating downstream neural activity[10,86,87]. Alternatively, vagal afferents expressing Piezo2 can directly respond to mechanical forces, enabling rapid neural signaling[85]. The co-expression of Piezo2 in both cell types suggests a multilayered mechanism for encoding gut distension. Future studies should aim to disentangle EEC-derived mechanosensation from direct activation of vagal afferents.

With access to the entire vagal population in larval zebrafish, we observed minimal response lateralization to distension, contrasting with the functional asymmetries of the left and right vagus observed in rodents[6,26,88]. This discrepancy may reflect underlying physical differences. Compared to the

anatomically asymmetric gastrointestinal tract of adult mammals and lateralized vagal innervation and function, the larval zebrafish gut is symmetrical[89,90], which may underlie the overall lack of functional lateralization in zebrafish. Investigating how gut anatomy and vagal function develop may reveal whether lateralized gut-brain signaling emerges in conjunction with bodily asymmetry.

A key yet underexplored feature of gut-brain communication is the temporal coding of visceral signals. By delivering repeated intraluminal stimuli, mimicking multiple bites, we uncovered a diversity of temporal dynamics in neural responses across vagal and hindbrain neurons. These response patterns demonstrate that enteric information about ongoing feeding status and history is relayed in neurons exhibiting sensitization, habituation, delayed onset, ramping, and selective responses to initial trials, revealing how neural dynamics evolve on a trial-by-trial basis (**Figure 6B**). Our data emphasize that interoceptive coding is inherently dynamic, and that uncovering the gut's influence on the brain requires attention to how signals unfold across time and experience.

Interestingly, we observed that enteric stimulation suppressed neural activity in subsets of vagal and hindbrain neurons. This is particularly noteworthy in vagal afferents, because activation in response to enteric stimuli has been extensively studied, while suppressive dynamics are rarely reported. A possible mechanism is that enteric stimuli engage GABA-expressing EECs[91,92] to suppress vagal sensory neurons[93,94]. Inhibitory signaling could thus act alongside excitatory glutamatergic inputs to balance neural activity by sharpening signal contrast[95,96]. Such modulation may be crucial for coordinating gut motility. For instance, vagal suppression may ensure that contraction in one gut region coincides with relaxation in another, facilitating directional transit. Supporting this, a recent study in the NTS demonstrated that stomach distension suppresses neurons responsive to intestinal distension, suggesting suppressive mechanisms may originate at the vagal sensory level[37]. Future studies using neurotransmitter-specific reporters or pharmacological tools could clarify how suppression plays a role in interoceptive coding.

Unexpectedly, we observed no significant topographic organization of enteric responses. While this aligns with findings in other larval zebrafish sensory systems, such as the lateral line[97], it contrasts with anesthetized mammalian models, where the NTS shows clear spatial separation of visceral responses[37]. However, a recent awake mouse study reported response patterns tied not to topography but to molecular identity, suggesting that functional organization under behaving conditions may differ from that observed under anesthesia[38]. Our awake imaging approach may thus reveal a more naturalistic pattern of visceral representation.

In these awake zebrafish, we demonstrate that gut distension alone is sufficient to elicit rapid and widespread neural responses across vagal and hindbrain neurons. Complementing a recent study in larval zebrafish that excluded mechanical cues and reported more spatially restricted responses[49], our findings suggest that including gut distension captures a more distributed pattern. This ubiquity of distension-responsive neurons underscores gut distension as the dominant visceral signal for fast neural communication during this developmental window.

Glucose and glycine in the gut evoked neural responses that were nearly indistinguishable from distension alone. While these results may be specific to the conditions tested, such as volume or concentration of delivered stimuli, these same concentrations were sufficient to elicit behavioral changes in our feeding assay. Therefore, it is likely that nutritive information is overshadowed by the dominant stretch signal shared across all stimuli. Systematically varying nutrient concentrations and decoupling mechanical from chemical cues will be essential to clarify how distension and nutrient identity interact to influence feeding-related brain activity.

Nonetheless, the aversive compound AITC triggered diverse neural dynamics with a unifying characteristic of a slow-onset response. The slower temporal profile mimics the dynamics of visceral pain signaling, which has a slower onset than somatic pain[98–100]. Zebrafish also use earlier sensory modalities such as olfaction[55,101,102], taste[71,103–105], and the lateral line[104,106] to avoid harmful substances pre-ingestion. Slow-onset gut signals may therefore function as a failsafe, activating post-ingestive defenses like excretion, emesis, or feeding cessation when earlier checkpoints fail to detect the threat.

Our results highlight that in early development, EECs in the gut epithelium already begin to shape feeding behavior by mediating nutrient-specific satiety signals to the brain. Among these post-ingestive signals transmitted via the gut-vagus-brain circuit, we found that rapid detection of gut volume changes and aversive stimuli takes precedence over identifying specific nutrient content. This prioritization likely reflects the need to rapidly assess how much has been ingested to meet the high and variable energy demands of early development[107,108], when individual gut capacities and intake can differ significantly[109–111]. As animals mature and their feeding strategies become more selective, we expect finer sensory discrimination mechanisms to gain prominence. While fast gut-brain communication is established in adult systems, our findings demonstrate that this essential survival strategy for evaluating ingestion begins far earlier in life than previously appreciated.

Resource availability

Lead contact

Further information and requests for resources and reagents should be directed to the lead contact, Eva A. Naumann (eva.naumann@duke.edu).

Materials availability

All the original reagents presented in this study are available from the lead contact on a reasonable request.

Data and code availability

All data reported in this paper will be shared by the lead contact upon request. All analyses were run on custom Python scripts, Jupyter notebooks, and GraphPad Prism files, available on https://gitlab.oit.duke.edu/ean26/arinel-et-al_2025. For calcium imaging analysis, the notebooks utilize our custom-written module at https://github.com/minel-arinel/caImageAnalysis. The notebooks for alignment use another environment and repository, which can be found at https://github.com/minel-arinel/alignment. Detailed instructions for executing the analysis notebooks and replicating published results are provided in our manuscript repository.

Acknowledgements

We would like to thank J. Rawls, L. Ye, and M. Morash for providing transgenic lines, training in the original gavage method, and insightful discussions and feedback; A. Oesterle for assistance in optimizing gavage needle production; the Bagnat Lab for microforge access; A. Pellegrino for assistance with sliceTCA optimization and calculations related to goodness-of-fit and sparsity; the Bohórquez Lab for insightful discussions on gut-brain sensory biology; and K. Abdelaal for feedback on experiments, figures, and the manuscript. We would also like to thank J. Burris, K. Olivera, and L. Frauen for zebrafish husbandry. This work was supported by a Boehringer Ingelheim Fonds PhD fellowship to M.A., as well as a Duke Institute of Brain Sciences Research Incubator Award and an Alfred P. Sloan Foundation Research Fellowship to E.A.N.

Author contributions

M.A. and E.A.N. conceived the project. M.A. validated the novel transgenic lines and was responsible for conducting and analyzing all gavage experiments. M.A. also developed the gavage methodology, with assistance from K.M.M.. J.A. conducted the gut-mediated feeding experiments and handled the crossing of zebrafish lines for all experiments. J.A. and E.P.D. generated the new transgenic zebrafish lines. M.H. created all the complex particles used in the feeding experiments. M.A. and E.A.N. wrote the manuscript and prepared the figures with feedback from all contributing authors.

Declaration of interests

The authors declare no competing interests.

Experimental model and study participant details

Animals

For all experiments, we used 6–10 dpf zebrafish as their gastrointestinal tract is functional[112], and the yolk sac is depleted[113] at this age. Zebrafish are obtained as fertilized embryos from adult breeders, maintained at a 14/10 hour light/dark cycle at 28.5°C. Groups of ~30 embryos were raised in pH-buffered, filtered E3 medium (5 mM NaCl, 0.55 mM $CaSO_4$, 0.45 mM $NaHCO_3$). Starting at 4 dpf, the zebrafish were fed daily with live paramecia. For feeding behavior experiments, we used Casper zebrafish, which lack dark melanophores and reflective iridophores on the skin[114]. We tested the effects of EEC depletion on feeding in outcrosses of *Tg(neurod1:cre; cmlc2:EGFP)*^{rdu79} and *TgBAC(gata5:loxP-mCherry-STOP-loxP-DTA)*^{pd315} EK (Ekwil) zebrafish, which express diphtheria toxin (DTA) in most of the EECs located in the proximal and midgut[43]. For anatomical imaging of EECs and vagal fibers (**Figure 2A**), we outcrossed *Tg(-5kbneurod1:TagRFP)*^{w69}[115] to *Tg(isl1:EGFP)*^{rw0}[116]. For two-photon imaging in vagal neurons and hindbrain, we generated two novel transgenic lines, *Tg(elavl3:H2B-GCaMP8m)* in the Casper background with nuclear-localized expression of the calcium sensor GCaMP8m *and Tg(neurod1:GCaMP8m-SV40)* with standard molecular cloning techniques (**Supplementary methods**). All experiments were approved by Duke University School of Medicine's Institutional Animal Care and Use Committee (IACUC, Protocol Registry Number A058-24-03).

Method details

Gut-mediated feeding assay

To test gut-mediated feeding, we developed a behavioral assay using complex particles (CPs), which are odorless, alginate-encapsulated liposomes that release nutrients post-ingestion. CPs were produced as previously described[53,117] in the 50–150 µm size range (**Supplementary methods**). We separated 8-dpf sibling zebrafish into new petri dishes of control and nutrient groups (maximum 20 larvae per dish), each containing 55 mL of E3 medium. After 24 hours of fasting, we introduced 18 mL of CP solution into each dish for a final concentration of 0.05 mg/mL. Control particles contained only sodium fluorescein as a negative control. Test particles contained sodium chloride (NaCl), D-(+)-glucose, glycine, or L-alanine (**Table S1**). Particle solutions were prepared at a concentration of 0.2 mg/mL in E3 medium and stored at 4°C and warmed to room temperature 30 minutes before each experiment. CP solutions were filtered using a 70 µm strainer (76327-100, VWR) to remove large particles. Three experiments were conducted without filtering, but showed no significant effect on feeding (see "Feeding behavior data processing and analysis"). After free feeding for 45 minutes, zebrafish were transferred into 50 mL falcon tubes containing 20 mL E3 medium and placed on ice. Post-euthanasia, E3 medium was replaced with 10 mL of 4% (w/v) paraformaldehyde (PFA; 047340.9M, Thermo Scientific) in 1X phosphate-buffered saline (119-069-101, Quality Biological) for fixation. After an hour, the fish were moved to 15 mL falcon tubes containing 10 mL of 0.1% Triton X-100 (9002-93-1, MP Biomedicals) in E3 medium for repeated washing. Individual zebrafish were either immediately embedded on their side in 1.5% (w/v) low-melting-point agarose (16520-050, Invitrogen) or stored overnight at 4°C for next-day imaging. Side-view images were captured using a stereo microscope (MVX10, Olympus) at 6.3X zoom with blue light illumination (X-Cite mini+ Compact, Excelitas) and a smartphone (iPhone SE, Apple) with a phone-to-eyepiece adapter (Gosky, https://www.amazon.com/gp/product/B013D2ULO6). All images were recorded with the ProCam app[118], setting shutter speed to 1/10 seconds, ISO at 2112, and white balance at 4400K. Images were saved directly as TIFF files at resolutions of 3024x3024 pixels for square images and 4032x3024 for 4:3 ratio images.

Feeding behavior data processing and analysis

After acquisition, images were imported to Fiji as separate TIFF files. For each fish, we selected the entire gut area, avoiding autofluorescence from the swim bladder, particles in the esophagus that have not reached the gut, or debris outside the fish. The cropped gut images were saved as separate 8-bit grayscale TIFF files. Applying a conservative threshold to extract only the particles, we used custom Python code to analyze fluorescence intensity values per fish. To assess whether CP filtration affected the results, we performed a bootstrapping analysis comparing the gut fluorescence of controls of filtered and unfiltered experiments. Across 1000 iterations, we found no significant difference between filtered and unfiltered conditions (median $P = 0.3937$, Kolmogorov-Smirnov test), so we combined all datasets. Only fish with fluorescence in their gut were included in pixel intensity analyses, reflecting active feeding behavior. To determine batch variability in consumption, we compared raw fluorescence values of control particles across experiments (**Figure S1B and S1D**), which showed significant batch effects ($P < 0.0001$, Kruskal-Wallis test). Therefore, we normalized raw pixel intensity values to the median of each experiment's control distribution.

Microgavage during two-photon imaging

Microgavage needle preparation:

To record neural activity in response to enteric stimulation, we adapted the zebrafish microgavage procedure[63] to deliver precise amounts of nutrients to the intestinal lumen of awake zebrafish during two-photon imaging. To prepare custom microgavage needles, we used a pipette puller (P-1000, Sutter Instrument) with 1.0 mm aluminosilicate glass (AF100-64-10, Sutter Instrument), which is stronger and more flexible than borosilicate[119]. Needles were clipped to an outer diameter of ≤20 µm using the glass-on-glass technique[119], bent 30° 0.5 mm from the tip, and lightly fire-polished using a microforge (MF2, Narishige). On each experimental day, individual gavage needles were back-filled with mineral oil (M5904, Sigma-Aldrich), using a 1 cc syringe (748019-0001, Kimble) connected to a pipette filler (MF28G-5, World Precision Instruments), removing any air bubbles. Once filled, each needle was attached to a holder, which is linked directly to a separate syringe barrel (910-N, Metcal), itself connected to an injector (DX-250, Metcal). The needle and syringe assembly were then mounted on a manual micromanipulator (M-152, Narishige). 1 µL of phenol red (P0290, Sigma-Aldrich) was mixed with 4 µL of the selected stimulus on parafilm. <1 µL of this solution was then front-filled into the needle. To calibrate the injection volume, the injector air pressure and time were adjusted to result in consistent 2 nL ejections without any capillary action (**Supplementary methods**).

Stimulus preparation for gavage:

For stretch-only experiments, gavage needles were filled with E3 medium. For chemical stimuli, 31.25 mM solutions were prepared and mixed 1:4 with phenol red (P0290, Sigma-Aldrich) to yield a final concentration of 25 mM. D-(+)-glucose (G7021, Sigma-Aldrich) and glycine (G7126, Sigma-Aldrich) were dissolved in E3 medium, while allyl isothiocyanate (AITC; 377430, Sigma-Aldrich) was prepared in 1X phosphate-buffered saline (70011-044, Gibco) to ensure solubility[43].

Microgavage during calcium imaging:

We selected 6–10 dpf *Tg(elavl3:H2B-GCaMP8m)* zebrafish with bright expression. Depending on the experiment, we embedded individuals either sideways (vagal imaging) or dorsal side up (hindbrain imaging) in the center of a 55 mm petri dish's lid, onto a layer of 1.5% (w/v) low-melting-point agarose (16520-050, Invitrogen). After flooding the dish with E3 medium, a fine scalpel (08-924-20, FEATHER 715) removed agarose around the fish's mouth. We used a larger scalpel (MPR-47101, MedPride) to cleanly trim agarose on both sides of the fish, ensuring the proper position of a right-angle prism mirror with anti-reflective coating on its legs (PS910L-B, Thorlabs) and minimal obstruction for the infrared light. After positioning of the fish under the two-photon objective, the syringe barrel with the gavage needle was mounted onto a motorized micromanipulator (MP-865, Sutter Instrument) on a custom acrylic stage.

With an infrared light (M780L3, Thorlabs) directed at the prism, we captured images through a 45° hot mirror (43-958, Edmund Optics) reflecting light towards an infrared camera (1800 U-2050m, Allied Vision). Guided by the dual view of anatomical landmarks, including the mouth, heart, swim bladder, otolith, gut, and pharynx, the gavage needle was inserted into the mouth without harming the fish. Using fine control of the micromanipulator, the needle was gently moved past the esophagus into the proximal gut, monitoring the fish's heartbeat and watching for signs of twitching, indicating potential injury. Each experiment started by recording a 5-minute baseline calcium activity in vagal or hindbrain populations, followed by five injections administered at 2-minute intervals, and an additional 2-minute recording. After each gavage, we slowly retracted the needle using the micromanipulator. Afterwards, we examined each fish under a stereo microscope to confirm that the phenol red is localized only within the gut. Checking for normal heart rate, liver morphology, and jaw integrity, fish were released from the agarose to assess their motor behavior.

Two-photon calcium imaging

To record neural activity in live zebrafish, we used a two-photon laser-scanning microscope (Ultima2Pplus, Bruker) with a 20X objective (XLUMPLFLN20XW, Olympus). Fluorescent images were captured using a pulsed femtosecond laser (Axon 920-2 TPC, Coherent) as excitation source, at a power of 23 mW on the specimen. For functional volumetric recordings, we imaged at a resolution of 512x512 pixels, covering 200.5 µm x 200.5 µm for vagal and 267.3 µm x 267.3 µm for brain recordings. We averaged 4 frames per acquisition, achieving a final rate of ~1.3 Hz. Using resonant scanning, we recorded 5 planes volumetrically, spaced 10 µm apart, in either left or right vagal neurons or hindbrain, identified using anatomical landmarks in the *Tg(elavl3:H2B-GCaMP8m)* line. At the end of each imaging session, we captured a high-resolution (1024x1024 pixels) anatomy stack from 10 µm above to 10 µm below the targeted imaging planes, at intervals of 2.5 µm. Left and right vagal ganglion imaging was performed in separate fish due to anatomical separation.

Two-photon data processing and analysis

Following data acquisition, we preprocessed and aligned uncompressed image volumes with their corresponding timestamps for gavage injections, for analysis of individual planes. Using CaImAn[120], we performed motion correction with NoRMCorre[121] and source extraction with constrained non-negative matrix factorization (CNMF)[122]. Parameters were optimized via `mesmerize-core` (https://github.com/nel-lab/mesmerize-core). The resulting sources, referred to as neurons, were filtered based on criteria such as location, temporal peaks, and proximity to other neurons. To observe spatial organization, we aligned each recording to an anatomical reference image using reverse alignment with SimpleITK[123–125].

All heatmaps display denoised traces, sorted by the onset of its maximum response. From these data, we characterized five temporal characteristics: (1) peak dF/F normalized to the pre-injection baseline of the first trial (pre), (2) peak dF/F normalized to the pre-injection period of each trial (pre-inj.), (3) baseline area under the curve (AUC), (4) time at half-maximum, and (5) time to decay (**Figures S4C and S4D**, **Supplementary methods**). We used Spearman rank-order correlation on the peak dF/F (pre) values to categorize neurons as "integrating" or "habituating" ($P<0.05$) (**Figure S4E**). Remaining non-significant neurons were categorized as "monotonic". We focused on subtypes and regions with at least 10 neurons total for vagal recordings or 10 neurons per fish for hindbrain regions (**Figure S7**).

Slice tensor component analysis (sliceTCA)

Data preprocessing:
To focus sliceTCA dimensionality reduction on the post-injection period, we extracted traces from 4 frames before and 20 after each injection of responsive neurons. Since some zebrafish only received four injections, we focused on the first four pulses. All traces were smoothed with a Gaussian filter along

the time axis (σ=1) and normalized to the overall standard deviation so that the mean squared error corresponded to the unexplained variance.

Cross-validated model selection:
To choose the number of components in each slice type, we ran a 3D grid search to optimize the cross-validated loss[65]. We masked 20% of the entries as held-out data, chosen in randomly selected 7-frame blocks (~5.3 s) of consecutive time points in random neurons and trials. Blocked masking of held-out data was done to avoid temporal correlations between the training and testing data due to the slow dynamics of the calcium indicator. To protect further against spuriously high cross-validation performance due to temporal correlations, we trimmed the first 2 frames (~1.5 s) from each block. These data were discarded from the test set, and only the remaining interior of each block was used to calculate the cross-validated loss. We repeated the grid search ten times with different random seeds for train-test split and parameter initialization. We used a learning rate of 0.001, maximum iterations of 10000, and minimum standard deviation of 10^{-4}. We ran non-constrained sliceTCA that allowed both positive and negative weights. Admissible models were defined as those achieving a minimum of 95% of the optimal performance. We selected the model by identifying the number of components that (1) generated a plateaued average test loss, (2) reconstructed all neurons with positive goodness-of-fit, and (3) had the highest sparsity across neuron weights.

Reconstruction performance:
For each neuron, we estimated the goodness of fit of the sliceTCA reconstruction (**Figure 5G**)[65]:

$$1 - \frac{\sum_{t,k}(X_{n,t,k} - \hat{X}_{n,t,k})^2}{\sum_{t,k} X_{n,t,k}^2}$$

where X is the input data and $\hat{X}$ is the reconstructed data at neuron n, time t, and trial k. This goodness of fit asks how much of the neuron's total activity is explained by the reconstruction. However, if a neuron has high overall activity, it can achieve high goodness of fit even if the model just tracks mean trends. If a neuron exhibits low temporal variance then small reconstruction errors appear disproportionately large. Therefore, for model selection (**Figure S13C**), we compared the model error to the variance of each neuron's activity:

$$1 - \frac{\frac{1}{TK}\sum_{t,k}(X_{n,t,k} - \hat{X}_{n,t,k})^2}{var(X_n)}$$

where T is the total number of time points and K is the total number of trials. With this, we can instead ask how well the reconstruction explains fluctuations in activity compared to just using the average response. If this goodness of fit is negative, it indicates that the model is worse than predicting the mean. Therefore, models with negative values in this goodness of fit calculation are eliminated.

Sparsity:
For model selection, we calculated the sparsity of the neuron component weights for each neuron (**Figure S13D**):

$$\frac{\sqrt{N} - \frac{\|R\|_1}{\|R\|_2}}{\sqrt{N} - 1}$$

where N is the number of neuron components, R is the vector of component weights for a single neuron, $\|R\|_1$ is the sum of absolute values (i.e., L^1 norm or Manhattan distance), and $\|R\|_2$ is the square root of the sum of squares (i.e., L^2 norm or Euclidean distance):

$$\|R\|_1 = \sum_{i=1}^{N} |R_i|$$

$$\|R\|_2 = \sqrt{\sum_{i=1}^{N} R_i^2}$$

This sparsity metric ranges from 0 (i.e., dense) to 1 (i.e., sparse), with high sparsity when a neuron's component weights are dominated by just a few nonzero entries.

Neuron clustering:
Each neuron was assigned to the component for which it had the highest absolute neuron weight. Because weights can be positive or negative, each of the four components was divided into two clusters based on weight polarity, resulting in eight total clusters. To analyze temporal dynamics, neuronal responses were averaged within each cluster (**Figures 5J** and **S14**). Stimulus contributions to each cluster were assessed by plotting the distributions of absolute neuron weights using split violin plots (**Figure 5J**).

Quantification and statistical analysis

Statistical analyses were conducted with Python scripts or GraphPad Prism (version 10.4.1). Detailed outline of our statistical analysis strategy can be found in **Table S3**. Data were evaluated for normality using the appropriate normality test. Normally distributed datasets were run with parametric statistical tests, whereas non-normally distributed datasets were run with nonparametric statistical tests. For comparing two datasets, we checked for the similarity of variances. For comparing more than two normally distributed datasets, we checked for the similarity of standard deviations using the Brown-Forsythe test.

For non-normal datasets with two independent variables without repeated measures, we fit a generalized linear model (GLM; **Table S2**). For comparing percentages (**Figures 1H**, **S10C**, and **S11C**), since they have a lower and upper bound (0-100%), we ran GLMs with a beta regression. The percentages were brought to be in the range (0, 1), and to avoid having exactly 0 and 1 values, we further transformed the data according to Smithson and Verkuilen (2006)[126]:

$$y_i^* = \frac{y_i \times (N - 1) + s}{N}$$

where $y_i \in [0, 1]$ is the original percentage value divided by 100, N is the total number of values, $s \in (0, 1)$ is a small constant set to 0.5 for our calculations, and $y_i^* \in (0, 1)$ is the resulting value that avoids exact zeros or ones that the beta distribution cannot handle. For all other distributions, which are skewed and continuous, we used a Gamma GLM with a log link. Since some values, such as fold change (**Figures 1F and 1I**) or peak dF/F (**Figures S10E** and **S11G**) can be negative, all the values were shifted by the same number to be positive. A significant interaction or main effect was followed up with the appropriate multiple comparisons test. In our feeding assay, relative gut fluorescence values of WT and EEC^{DTA} had no significant differences between genotypes across stimuli, so we ran separate Kruskal-Wallis tests (**Figures 1F and 1I**; **Table S2**).

Results of statistical tests can be found on https://gitlab.oit.duke.edu/ean26/arinel-et-al_2025 and **Table S2**. All results are reported as mean ± standard error of the mean unless specified otherwise. Sample sizes were not predetermined by power analyses but were informed by preliminary experiments that evaluated the variance and effect sizes. Randomization and blinding to experimental conditions were not implemented during data collection or analysis.

References

1. Kaelberer, M.M., Rupprecht, L.E., Liu, W.W., Weng, P., and Bohórquez, D.V. (2020). Neuropod Cells: Emerging Biology of the Gut-Brain Sensory Transduction. Annu. Rev. Neurosci. https://doi.org/10.1146/annurev-neuro-091619-022657.
2. Liddle, R.A. (2019). Neuropods. Cell Mol Gastroenterol Hepatol *7*, 739–747. https://doi.org/10.1016/j.jcmgh.2019.01.006.
3. Tobias, A., and Sadiq, N.M. (2022). Physiology, Gastrointestinal Nervous Control. In StatPearls [Internet] (StatPearls Publishing).
4. Xie, Z., Zhang, X., Zhao, M., Huo, L., Huang, M., Li, D., Zhang, S., Cheng, X., Gu, H., Zhang, C., et al. (2022). The gut-to-brain axis for toxin-induced defensive responses. Cell *185*, 4298-4316.e21. https://doi.org/10.1016/j.cell.2022.10.001.
5. Bai, L., Sivakumar, N., Yu, S., Mesgarzadeh, S., Ding, T., Ly, T., Corpuz, T.V., Grove, J.C., Jarvie, B.C., and Knight, Z.A. (2022). Enteroendocrine cell types that drive food reward and aversion. eLife *11*, e74964. https://doi.org/10.7554/eLife.74964.
6. Han, W., Tellez, L.A., Perkins, M.H., Perez, I.O., Qu, T., Ferreira, J., Ferreira, T.L., Quinn, D., Liu, Z.-W., Gao, X.-B., et al. (2018). A Neural Circuit for Gut-Induced Reward. Cell *175*, 665-678.e23. https://doi.org/10.1016/j.cell.2018.08.049.
7. Jena, A., Montoya, C.A., Mullaney, J.A., Dilger, R.N., Young, W., McNabb, W.C., and Roy, N.C. (2020). Gut-Brain Axis in the Early Postnatal Years of Life: A Developmental Perspective. Front. Integr. Neurosci. *14*. https://doi.org/10.3389/fnint.2020.00044.
8. Muhammad, F., Fan, B., Wang, R., Ren, J., Jia, S., Wang, L., Chen, Z., and Liu, X.-A. (2022). The Molecular Gut-Brain Axis in Early Brain Development. Int J Mol Sci *23*, 15389. https://doi.org/10.3390/ijms232315389.
9. Latorre, R., Sternini, C., Giorgio, R.D., and Meerveld, B.G.-V. (2016). Enteroendocrine cells: a review of their role in brain–gut communication. Neurogastroenterology & Motility *28*, 620–630. https://doi.org/10.1111/nmo.12754.
10. Alcaino, C., Knutson, K.R., Treichel, A.J., Yildiz, G., Strege, P.R., Linden, D.R., Li, J.H., Leiter, A.B., Szurszewski, J.H., Farrugia, G., et al. (2018). A population of gut epithelial enterochromaffin cells is mechanosensitive and requires Piezo2 to convert force into serotonin release. Proceedings of the National Academy of Sciences *115*, E7632–E7641. https://doi.org/10.1073/pnas.1804938115.
11. Barton, J.R., Londregan, A.K., Alexander, T.D., Entezari, A.A., Covarrubias, M., and Waldman, S.A. (2023). Enteroendocrine cell regulation of the gut-brain axis. Front. Neurosci. *17*. https://doi.org/10.3389/fnins.2023.1272955.
12. Arinel, M., and Abdelaal, K. (2025). The gut and heart's role in reward processing. Front. Integr. Neurosci. *19*. https://doi.org/10.3389/fnint.2025.1479923.
13. Kaelberer, M.M., and Bohórquez, D.V. (2018). The now and then of gut-brain signaling. Brain Research *1693*, 192–196. https://doi.org/10.1016/j.brainres.2018.03.027.
14. Barakat, G.M., Ramadan, W., Assi, G., and Khoury, N.B.E. (2024). Satiety: a gut–brain–relationship. The Journal of Physiological Sciences *74*, 11. https://doi.org/10.1186/s12576-024-00904-9.
15. Bohórquez, D.V., Samsa, L.A., Roholt, A., Medicetty, S., Chandra, R., and Liddle, R.A. (2014). An Enteroendocrine Cell – Enteric Glia Connection Revealed by 3D Electron Microscopy. PLOS ONE *9*, e89881. https://doi.org/10.1371/journal.pone.0089881.
16. Buchanan, K.L., Rupprecht, L.E., Kaelberer, M.M., Sahasrabudhe, A., Klein, M.E., Villalobos, J.A., Liu, W.W., Yang, A., Gelman, J., Park, S., et al. (2022). The preference for sugar over sweetener depends on a gut sensor cell. Nat Neurosci, 1–10. https://doi.org/10.1038/s41593-021-00982-7.
17. Bellono, N.W., Bayrer, J.R., Leitch, D.B., Castro, J., Zhang, C., O'Donnell, T.A., Brierley, S.M., Ingraham, H.A., and Julius, D. (2017). Enterochromaffin Cells Are Gut Chemosensors that Couple to Sensory Neural Pathways. Cell *170*, 185-198.e16. https://doi.org/10.1016/j.cell.2017.05.034.

18. Psichas, A., Reimann, F., and Gribble, F.M. (2015). Gut chemosensing mechanisms. J Clin Invest *125*, 908–917. https://doi.org/10.1172/JCI76309.
19. Barton, J.R., Londregan, A.K., Alexander, T.D., Entezari, A.A., Bar-Ad, S., Cheng, L., Lepore, A.C., Snook, A.E., Covarrubias, M., and Waldman, S.A. (2023). Intestinal neuropod cell GUCY2C regulates visceral pain. J Clin Invest *133*. https://doi.org/10.1172/JCI165578.
20. Yamada, S., Natsubori, A., Harada, K., Tsuboi, T., and Monai, H. (2025). Immediate glucose signaling transmitted via the vagus nerve in gut–brain neural communication. iScience *28*. https://doi.org/10.1016/j.isci.2025.112439.
21. Bodnar, R.J., Castillo, A., Carata, I., Bochner, Y., Sarker, J., Rayman, N., Narine, S., Pines, R., Limbu, B., and Sclafani, A. (2025). Role of glutamatergic signaling in the acquisition and expression of learned sugar preferences in C57BL/6 mice. Physiol Behav *290*, 114748. https://doi.org/10.1016/j.physbeh.2024.114748.
22. Prescott, S.L., and Liberles, S.D. (2022). Internal senses of the vagus nerve. Neuron *110*, 579–599. https://doi.org/10.1016/j.neuron.2021.12.020.
23. Berthoud, H.-R., and Neuhuber, W.L. (2000). Functional and chemical anatomy of the afferent vagal system. Autonomic Neuroscience: Basic and Clinical *85*, 1–17. https://doi.org/10.1016/S1566-0702(00)00215-0.
24. Li, M., Tan, H.-E., Lu, Z., Tsang, K.S., Chung, A.J., and Zuker, C.S. (2022). Gut–brain circuits for fat preference. Nature *610*, 722–730. https://doi.org/10.1038/s41586-022-05266-z.
25. Tan, H.-E., Sisti, A.C., Jin, H., Vignovich, M., Villavicencio, M., Tsang, K.S., Goffer, Y., and Zuker, C.S. (2020). The gut–brain axis mediates sugar preference. Nature *580*, 511–516. https://doi.org/10.1038/s41586-020-2199-7.
26. Welch, H.F., Sankaranarayanan, I., Hong, V.M., Mazhar, K., Kolber, B.J., Price, T.J., and Thorn, C.A. (2024). Lateralized nodose ganglia gene expression implicates cholecystokinin receptors in interoceptive reward signaling. Preprint at bioRxiv, https://doi.org/10.1101/2024.11.01.621506 https://doi.org/10.1101/2024.11.01.621506.
27. de Araujo, A., Singh, A., McDougle, M., Braga, I., Leme, G., and de Lartigue, G. (2022). Asymmetric Control of Food Intake by Left and Right Vagal Sensory Neurons. The FASEB Journal *36*. https://doi.org/10.1096/fasebj.2022.36.S1.00R53.
28. Chen, J., Cheng, M., Wang, L., Zhang, L., Xu, D., Cao, P., Wang, F., Herzog, H., Song, S., and Zhan, C. (2020). A Vagal-NTS Neural Pathway that Stimulates Feeding. Current Biology *30*, 3986-3998.e5. https://doi.org/10.1016/j.cub.2020.07.084.
29. Borgmann, D., Ciglieri, E., Biglari, N., Brandt, C., Cremer, A.L., Backes, H., Tittgemeyer, M., Wunderlich, F.T., Brüning, J.C., and Fenselau, H. (2021). Gut-brain communication by distinct sensory neurons differently controls feeding and glucose metabolism. Cell Metabolism *33*, 1466-1482.e7. https://doi.org/10.1016/j.cmet.2021.05.002.
30. Brierley, D.I., Holt, M.K., Singh, A., de Araujo, A., McDougle, M., Vergara, M., Afaghani, M.H., Lee, S.J., Scott, K., Maske, C., et al. (2021). Central and peripheral GLP-1 systems independently suppress eating. Nat Metab *3*, 258–273. https://doi.org/10.1038/s42255-021-00344-4.
31. Alhadeff, A.L., Rupprecht, L.E., and Hayes, M.R. (2012). GLP-1 Neurons in the Nucleus of the Solitary Tract Project Directly to the Ventral Tegmental Area and Nucleus Accumbens to Control for Food Intake. Endocrinology *153*, 647–658. https://doi.org/10.1210/en.2011-1443.
32. Davis, S.F., Derbenev, A.V., Williams, K.W., Glatzer, N.R., and Smith, B.N. (2004). Excitatory and inhibitory local circuit input to the rat dorsal motor nucleus of the vagus originating from the nucleus tractus solitarius. Brain Res *1017*, 208–217. https://doi.org/10.1016/j.brainres.2004.05.049.
33. Zhang, C., Kaye, J.A., Cai, Z., Wang, Y., Prescott, S.L., and Liberles, S.D. (2021). Area Postrema Cell Types that Mediate Nausea-Associated Behaviors. Neuron *109*, 461-472.e5. https://doi.org/10.1016/j.neuron.2020.11.010.
34. Williams, E.K., Chang, R.B., Strochlic, D.E., Umans, B.D., Lowell, B.B., and Liberles, S.D. (2016). Sensory Neurons that Detect Stretch and Nutrients in the Digestive System. Cell *166*, 209–221. https://doi.org/10.1016/j.cell.2016.05.011.
35. Jameson, K.G., Kazmi, S.A., Ohara, T.E., Son, C., Yu, K.B., Mazdeyasnan, D., Leshan, E., Vuong, H.E., Paramo, J., Lopez-Romero, A., et al. (2025). Select microbial metabolites in the small intestinal lumen regulates vagal activity via receptor-mediated signaling. iScience *28*. https://doi.org/10.1016/j.isci.2024.111699.
36. Huerta, T.S., Chen, A.C., Chaudhry, S., Tynan, A., Morgan, T., Park, K., Adamovich-Zeitlin, R., Haider, B., Li, J.H., Nagpal, M., et al. (2025). Neural representation of cytokines by vagal sensory neurons. Nat Commun *16*, 3840. https://doi.org/10.1038/s41467-025-59248-6.

37. Ran, C., Boettcher, J.C., Kaye, J.A., Gallori, C.E., and Liberles, S.D. (2022). A brainstem map for visceral sensations. Nature *609*, 320–326. https://doi.org/10.1038/s41586-022-05139-5.
38. Wang, H., Lou, R., Wang, Y., Hao, L., Wang, Q., Li, R., Su, J., Liu, S., Zhou, X., Gao, X., et al. (2024). Parallel gut-to-brain pathways orchestrate feeding behaviors. Nat Neurosci, 1–16. https://doi.org/10.1038/s41593-024-01828-8.
39. Veldman, M.B., and Lin, S. (2008). Zebrafish as a Developmental Model Organism for Pediatric Research. Pediatr Res *64*, 470–476. https://doi.org/10.1203/PDR.0b013e318186e609.
40. Ng, A.N.Y., de Jong-Curtain, T.A., Mawdsley, D.J., White, S.J., Shin, J., Appel, B., Dong, P.D.S., Stainier, D.Y.R., and Heath, J.K. (2005). Formation of the digestive system in zebrafish: III. Intestinal epithelium morphogenesis. Developmental Biology *286*, 114–135. https://doi.org/10.1016/j.ydbio.2005.07.013.
41. Wallace, K.N., Akhter, S., Smith, E.M., Lorent, K., and Pack, M. (2005). Intestinal growth and differentiation in zebrafish. Mechanisms of Development *122*, 157–173. https://doi.org/10.1016/j.mod.2004.10.009.
42. Ye, L., Mueller, O., Bagwell, J., Bagnat, M., Liddle, R.A., and Rawls, J.F. (2019). High fat diet induces microbiota-dependent silencing of enteroendocrine cells. eLife *8*, e48479. https://doi.org/10.7554/eLife.48479.
43. Ye, L., Bae, M., Cassilly, C.D., Jabba, S.V., Thorpe, D.W., Martin, A.M., Lu, H.-Y., Wang, J., Thompson, J.D., Lickwar, C.R., et al. (2021). Enteroendocrine cells sense bacterial tryptophan catabolites to activate enteric and vagal neuronal pathways. Cell Host & Microbe *29*, 179-196.e9. https://doi.org/10.1016/j.chom.2020.11.011.
44. Wallace, K.N., and Pack, M. (2003). Unique and conserved aspects of gut development in zebrafish. Developmental Biology *255*, 12–29. https://doi.org/10.1016/S0012-1606(02)00034-9.
45. Li, J., Prochaska, M., Maney, L., and Wallace, K.N. (2020). Development and organization of the zebrafish intestinal epithelial stem cell niche. Developmental Dynamics *249*, 76–87. https://doi.org/10.1002/dvdy.16.
46. Sur, A., Wang, Y., Capar, P., Margolin, G., Prochaska, M.K., and Farrell, J.A. (2023). Single-cell analysis of shared signatures and transcriptional diversity during zebrafish development. Developmental Cell *58*, 3028-3047.e12. https://doi.org/10.1016/j.devcel.2023.11.001.
47. Wen, J., Mercado, G.P., Volland, A., Doden, H.L., Lickwar, C.R., Crooks, T., Kakiyama, G., Kelly, C., Cocchiaro, J.L., Ridlon, J.M., et al. (2021). Fxr signaling and microbial metabolism of bile salts in the zebrafish intestine. Science Advances *7*, eabg1371. https://doi.org/10.1126/sciadv.abg1371.
48. Alsudayri, A., Perelman, S., Brewer, M., Chura, A., McDevitt, M., Drerup, C., and Ye, L. (2024). Gut microbiota regulate maturation and mitochondrial function of the nutrient-sensing enteroendocrine cell. Development *151*, dev202544. https://doi.org/10.1242/dev.202544.
49. Chen, W., James, B., Ruetten, V.M.S., Banala, S., Wei, Z., Fleishman, G., Rubinov, M., Fishman, M.C., Engert, F., Lavis, L.D., et al. (2025). Whole-brain, all-optical interrogation of neuronal dynamics underlying gut interoception in zebrafish. Preprint at bioRxiv, https://doi.org/10.1101/2025.03.26.645305 https://doi.org/10.1101/2025.03.26.645305.
50. Vendrell-Llopis, N., and Yaksi, E. (2015). Evolutionary conserved brainstem circuits encode category, concentration and mixtures of taste. Sci Rep *5*, 17825. https://doi.org/10.1038/srep17825.
51. Kaneko, T., Boulanger-Weill, J., Isabella, A.J., and Moens, C.B. (2024). Position-independent functional refinement within the vagus motor topographic map. Cell Reports *43*. https://doi.org/10.1016/j.celrep.2024.114740.
52. Hawkyard, M., Stuart, K., Drawbridge, M., and Langdon, C. (2019). The early life stages of California yellowtail (Seriola dorsalis) and white seabass (Atractoscion nobilis) respond to food particle taste. Aquaculture *512*, 734285. https://doi.org/10.1016/j.aquaculture.2019.734285.
53. Hawkyard, M., Laurel, B., Barr, Y., Hamre, K., and Langdon, C. (2015). Evaluation of liposomes for the enrichment of rotifers (*Brachionus* sp.) with taurine and their subsequent effects on the growth and development of northern rock sole (*Lepidopsetta polyxystra*) larvae. Aquaculture *441*, 118–125. https://doi.org/10.1016/j.aquaculture.2015.02.012.
54. Lovett-Barron, M., Chen, R., Bradbury, S., Andalman, A.S., Wagle, M., Guo, S., and Deisseroth, K. (2020). Multiple convergent hypothalamus-brainstem circuits drive defensive behavior. Nat Neurosci *23*, 959–967. https://doi.org/10.1038/s41593-020-0655-1.
55. Herrera, K.J., Panier, T., Guggiana-Nilo, D., and Engert, F. (2021). Larval Zebrafish Use Olfactory Detection of Sodium and Chloride to Avoid Salt Water. Current Biology *31*, 782-793.e3. https://doi.org/10.1016/j.cub.2020.11.051.

56. Ren, X., Ferreira, J.G., Zhou, L., Shammah-Lagnado, S.J., Yeckel, C.W., and Araujo, I.E. de (2010). Nutrient Selection in the Absence of Taste Receptor Signaling. J. Neurosci. *30*, 8012–8023. https://doi.org/10.1523/JNEUROSCI.5749-09.2010.
57. Sclafani, A., Cardieri, C., Tucker, K., Blusk, D., and Ackroff, K. (1993). Intragastric glucose but not fructose conditions robust flavor preferences in rats. American Journal of Physiology-Regulatory, Integrative and Comparative Physiology *265*, R320–R325. https://doi.org/10.1152/ajpregu.1993.265.2.R320.
58. Zhang, L., Han, W., Lin, C., Li, F., and de Araujo, I.E. (2018). Sugar Metabolism Regulates Flavor Preferences and Portal Glucose Sensing. Front Integr Neurosci *12*, 57. https://doi.org/10.3389/fnint.2018.00057.
59. Webb, K.L., and Johannes, R.E. (1967). Studies of the Release of Dissolved Free Amino Acids by Marine Zooplankton. Limnology and Oceanography *12*, 376–382. https://doi.org/10.4319/lo.1967.12.3.0376.
60. Carr, W. e. s., Netherton, Iii., J.C., Gleeson, R.A., and Derby, C.D. (1996). Stimulants of Feeding Behavior in Fish: Analyses of Tissues of Diverse Marine Organisms. The Biological Bulletin *190*, 149–160. https://doi.org/10.2307/1542535.
61. Blumberg, M.S., Sokoloff, G., Tiriac, A., and Del Rio-Bermudez, C. (2015). A Valuable and Promising Method for Recording Brain Activity in Behaving Newborn Rodents. Dev Psychobiol *57*, 506–517. https://doi.org/10.1002/dev.21305.
62. Murata, Y., and Colonnese, M.T. (2020). GABAergic interneurons excite neonatal hippocampus in vivo. Science Advances *6*, eaba1430. https://doi.org/10.1126/sciadv.aba1430.
63. Cocchiaro, J.L., and Rawls, J.F. (2013). Microgavage of Zebrafish Larvae. JoVE (Journal of Visualized Experiments), e4434. https://doi.org/10.3791/4434.
64. Roberts, A.C., Alzagatiti, J.B., Ly, D.T., Chornak, J.M., Ma, Y., Razee, A., Zavradyan, G., Khan, U., Lewis, J., Natarajan, A., et al. (2020). Induction of Short-Term Sensitization by an Aversive Chemical Stimulus in Zebrafish Larvae. eNeuro *7*. https://doi.org/10.1523/ENEURO.0336-19.2020.
65. Pellegrino, A., Stein, H., and Cayco-Gajic, N.A. (2024). Dimensionality reduction beyond neural subspaces with slice tensor component analysis. Nat Neurosci *27*, 1199–1210. https://doi.org/10.1038/s41593-024-01626-2.
66. Spence, R., Fatema, M.K., Ellis, S., Ahmed, Z.F., and Smith, C. (2007). Diet, growth and recruitment of wild zebrafish in Bangladesh. Journal of Fish Biology *71*, 304–309. https://doi.org/10.1111/j.1095-8649.2007.01492.x.
67. Jeeja, P.K., Joseph, I., and Raj, R.P. (2011). Nutritional composition of rotifer (Brachionus plicatilis Muller) cultured using selected natural diets. Indian Journal of Fisheries *58*, 59–65.
68. Dabrowski, K., and Rusiecki, M. (1983). Content of total and free amino acids in zooplanktonic food of fish larvae. Aquaculture *30*, 31–42. https://doi.org/10.1016/0044-8486(83)90149-7.
69. Myers, K.P., and Sclafani, A. (2001). Conditioned enhancement of flavor evaluation reinforced by intragastric glucose: I: Intake acceptance and preference analysis. Physiology & Behavior *74*, 481–493. https://doi.org/10.1016/S0031-9384(01)00595-9.
70. Koide, T., Miyasaka, N., Morimoto, K., Asakawa, K., Urasaki, A., Kawakami, K., and Yoshihara, Y. (2009). Olfactory neural circuitry for attraction to amino acids revealed by transposon-mediated gene trap approach in zebrafish. Proc Natl Acad Sci U S A *106*, 9884–9889. https://doi.org/10.1073/pnas.0900470106.
71. Oike, H., Nagai, T., Furuyama, A., Okada, S., Aihara, Y., Ishimaru, Y., Marui, T., Matsumoto, I., Misaka, T., and Abe, K. (2007). Characterization of ligands for fish taste receptors. J Neurosci *27*, 5584–5592. https://doi.org/10.1523/JNEUROSCI.0651-07.2007.
72. Amole, N., and Unniappan, S. (2009). Fasting induces preproghrelin mRNA expression in the brain and gut of zebrafish, Danio rerio. Gen Comp Endocrinol *161*, 133–137. https://doi.org/10.1016/j.ygcen.2008.11.002.
73. Cummings, D.E., Purnell, J.Q., Frayo, R.S., Schmidova, K., Wisse, B.E., and Weigle, D.S. (2001). A preprandial rise in plasma ghrelin levels suggests a role in meal initiation in humans. Diabetes *50*, 1714–1719. https://doi.org/10.2337/diabetes.50.8.1714.
74. Morash, M., Kay, R.G., Soderblom, E.J., MacLean, G.H., Wen, J., Moore, P.J., Lickwar, C.R., Gribble, F.M., Reimann, F., Liddle, R.A., et al. (2025). Intestinal enteroendocrine cell subtype differentiation and hormone production in zebrafish. Preprint at bioRxiv, https://doi.org/10.1101/2025.01.17.633579 https://doi.org/10.1101/2025.01.17.633579.
75. Lavergne, A., Tarifeño-Saldivia, E., Pirson, J., Reuter, A.-S., Flasse, L., Manfroid, I., Voz, M.L., and Peers, B. (2020). Pancreatic and intestinal endocrine cells in zebrafish share common transcriptomic signatures and regulatory programmes. BMC Biology *18*, 109. https://doi.org/10.1186/s12915-020-00840-1.

76. Lu, V.B., Gribble, F.M., and Reimann, F. (2021). Nutrient-Induced Cellular Mechanisms of Gut Hormone Secretion. Nutrients *13*, 883. https://doi.org/10.3390/nu13030883.
77. Kaelberer, M.M., Buchanan, K.L., Klein, M.E., Barth, B.B., Montoya, M.M., Shen, X., and Bohórquez, D.V. (2018). A gut-brain neural circuit for nutrient sensory transduction. Science *361*. https://doi.org/10.1126/science.aat5236.
78. Coste, B., Mathur, J., Schmidt, M., Earley, T.J., Ranade, S., Petrus, M.J., Dubin, A.E., and Patapoutian, A. (2010). Piezo1 and Piezo2 Are Essential Components of Distinct Mechanically Activated Cation Channels. Science *330*, 55–60. https://doi.org/10.1126/science.1193270.
79. Marshall, K.L., Saade, D., Ghitani, N., Coombs, A.M., Szczot, M., Keller, J., Ogata, T., Daou, I., Stowers, L.T., Bönnemann, C.G., et al. (2020). PIEZO2 in sensory neurons and urothelial cells coordinates urination. Nature *588*, 290–295. https://doi.org/10.1038/s41586-020-2830-7.
80. Servin-Vences, M.R., Lam, R.M., Koolen, A., Wang, Y., Saade, D.N., Loud, M., Kacmaz, H., Frausto, S., Zhang, Y., Beyder, A., et al. (2023). PIEZO2 in somatosensory neurons controls gastrointestinal transit. Cell *186*, 3386-3399.e15. https://doi.org/10.1016/j.cell.2023.07.006.
81. Aragona, M., Mhalhel, K., Pansera, L., Montalbano, G., Guerrera, M.C., Levanti, M., Laurà, R., Abbate, F., Vega, J.A., and Germanà, A. (2024). Localization of Piezo 1 and Piezo 2 in Lateral Line System and Inner Ear of Zebrafish (Danio rerio). Int J Mol Sci *25*, 9204. https://doi.org/10.3390/ijms25179204.
82. Faucherre, A., Nargeot, J., Mangoni, M.E., and Jopling, C. (2013). piezo2b Regulates Vertebrate Light Touch Response. J. Neurosci. *33*, 17089–17094. https://doi.org/10.1523/JNEUROSCI.0522-13.2013.
83. Aragona, M., Mhalhel, K., Cometa, M., Franco, G.A., Montalbano, G., Guerrera, M.C., Levanti, M., Laurà, R., Abbate, F., Vega, J.A., et al. (2024). Piezo 1 and Piezo 2 in the Chemosensory Organs of Zebrafish (Danio rerio). Int J Mol Sci *25*, 7404. https://doi.org/10.3390/ijms25137404.
84. Kim, M., Heo, G., and Kim, S.-Y. (2022). Neural signalling of gut mechanosensation in ingestive and digestive processes. Nat Rev Neurosci *23*, 135–156. https://doi.org/10.1038/s41583-021-00544-7.
85. Mercado-Perez, A., and Beyder, A. (2022). Gut feelings: mechanosensing in the gastrointestinal tract. Nat Rev Gastroenterol Hepatol *19*, 283–296. https://doi.org/10.1038/s41575-021-00561-y.
86. Mercado-Perez, A., Hernandez, J.P., Fedyshyn, Y., Treichel, A.J., Joshi, V., Kossick, K., Betageri, K.R., Farrugia, G., Druliner, B., and Beyder, A. (2024). Piezo2 interacts with E-cadherin in specialized gastrointestinal epithelial mechanoreceptors. Journal of General Physiology *156*, e202213324. https://doi.org/10.1085/jgp.202213324.
87. Wang, F., Knutson, K., Alcaino, C., Linden, D.R., Gibbons, S.J., Kashyap, P., Grover, M., Oeckler, R., Gottlieb, P.A., Li, H.J., et al. (2017). Mechanosensitive ion channel Piezo2 is important for enterochromaffin cell response to mechanical forces. The Journal of Physiology *595*, 79–91. https://doi.org/10.1113/JP272718.
88. de Araujo, A.M., Braga, I., Leme, G., Singh, A., McDougle, M., Smith, J., Vergara, M., Yang, M., Lin, M., Khoshbouei, H., et al. (2023). Asymmetric control of food intake by left and right vagal sensory neurons. Preprint at bioRxiv, https://doi.org/10.1101/2023.05.08.539627 https://doi.org/10.1101/2023.05.08.539627.
89. Arun, C.P. (2004). The Importance of Being Asymmetric: The Physiology of Digesta Propulsion on Earth and in Space. Annals of the New York Academy of Sciences *1027*, 74–84. https://doi.org/10.1196/annals.1324.008.
90. Grzymkowski, J., Wyatt, B., and Nascone-Yoder, N. (2020). The twists and turns of left-right asymmetric gut morphogenesis. Development *147*, dev187583. https://doi.org/10.1242/dev.187583.
91. Jessen, K.R., Hills, J.M., and Limbrick, A.R. (1988). GABA immunoreactivity and 3H-GABA uptake in mucosal epithelial cells of the rat stomach. Gut *29*, 1549. https://doi.org/10.1136/gut.29.11.1549.
92. Oomori, Y., Iuchi, H., Ishikawa, K., Satoh, Y., and Ono, K. (1992). Gamma-aminobutyric acid immunoreactivity in the enterochromaffin cells of the rat stomach. Acta Anat (Basel) *145*, 127–131. https://doi.org/10.1159/000147353.
93. Smid, S.D., Young, R.L., Cooper, N.J., and Blackshaw, L.A. (2001). GABABR expressed on vagal afferent neurones inhibit gastric mechanosensitivity in ferret proximal stomach. American Journal of Physiology-Gastrointestinal and Liver Physiology *281*, G1494–G1501. https://doi.org/10.1152/ajpgi.2001.281.6.G1494.
94. Hyland, N.P., and Cryan, J.F. (2010). A Gut Feeling about GABA: Focus on GABAB Receptors. Front Pharmacol *1*, 124. https://doi.org/10.3389/fphar.2010.00124.
95. Raccuglia, D., McCurdy, L.Y., Demir, M., Gorur-Shandilya, S., Kunst, M., Emonet, T., and Nitabach, M.N. (2016). Presynaptic GABA Receptors Mediate Temporal Contrast Enhancement in Drosophila Olfactory Sensory Neurons and Modulate Odor-Driven Behavioral Kinetics. eNeuro *3*. https://doi.org/10.1523/ENEURO.0080-16.2016.

96. Hammett, S.T., Cook, E., Hassan, O., Hughes, C.-A., Rooslien, H., Tizkar, R., and Larsson, J. (2020). GABA, noise and gain in human visual cortex. Neurosci Lett *736*, 135294. https://doi.org/10.1016/j.neulet.2020.135294.
97. Velez-Angel, N., Lu, S., Fabella, B., Reagor, C.C., Brown, H.R., Vázquez, Y., Jacobo, A., and Hudspeth, A.J. (2025). Optogenetic interrogation of the lateral-line sensory system reveals mechanisms of pattern separation in the zebrafish brain. Preprint at bioRxiv, https://doi.org/10.1101/2025.02.07.637118 https://doi.org/10.1101/2025.02.07.637118.
98. Boezaart, A.P., Smith, C.R., Chembrovich, S., Zasimovich, Y., Server, A., Morgan, G., Theron, A., Booysen, K., and Reina, M.A. (2021). Visceral versus somatic pain: an educational review of anatomy and clinical implications. Reg Anesth Pain Med *46*, 629–636. https://doi.org/10.1136/rapm-2020-102084.
99. Masuoka, T., Kudo, M., Yamashita, Y., Yoshida, J., Imaizumi, N., Muramatsu, I., Nishio, M., and Ishibashi, T. (2017). TRPA1 Channels Modify TRPV1-Mediated Current Responses in Dorsal Root Ganglion Neurons. Front. Physiol. *8*. https://doi.org/10.3389/fphys.2017.00272.
100. Sikandar, S., and Dickenson, A.H. (2012). Visceral Pain – the Ins and Outs, the Ups and Downs. Curr Opin Support Palliat Care *6*, 17–26. https://doi.org/10.1097/SPC.0b013e32834f6ec9.
101. Hussain, A., Saraiva, L.R., Ferrero, D.M., Ahuja, G., Krishna, V.S., Liberles, S.D., and Korsching, S.I. (2013). High-affinity olfactory receptor for the death-associated odor cadaverine. Proceedings of the National Academy of Sciences *110*, 19579–19584. https://doi.org/10.1073/pnas.1318596110.
102. Masuda, M., Ihara, S., Mori, N., Koide, T., Miyasaka, N., Wakisaka, N., Yoshikawa, K., Watanabe, H., Touhara, K., and Yoshihara, Y. (2024). Identification of olfactory alarm substances in zebrafish. Current Biology *34*, 1377-1389.e7. https://doi.org/10.1016/j.cub.2024.02.003.
103. Levanti, M., Randazzo, B., Viña, E., Montalbano, G., Garcia-Suarez, O., Germanà, A., Vega, J.A., and Abbate, F. (2016). Acid-sensing ion channels and transient-receptor potential ion channels in zebrafish taste buds. Annals of Anatomy - Anatomischer Anzeiger *207*, 32–37. https://doi.org/10.1016/j.aanat.2016.06.006.
104. Mojib, N., Xu, J., Bartolek, Z., Imhoff, B., McCarty, N.A., Shin, C.H., and Kubanek, J. (2017). Zebrafish aversive taste co-receptor is expressed in both chemo- and mechanosensory cells and plays a role in lateral line development. Sci Rep *7*, 13475. https://doi.org/10.1038/s41598-017-14042-3.
105. Boyer, B., Ernest, S., and Rosa, F. (2013). Egr-1 induction provides a genetic response to food aversion in zebrafish. Front Behav Neurosci *7*, 51. https://doi.org/10.3389/fnbeh.2013.00051.
106. Desban, L., Roussel, J., Mirat, O., Lejeune, F.-X., Keiser, L., Michalski, N., and Wyart, C. (2022). Lateral line hair cells integrate mechanical and chemical cues to orient navigation. Preprint at bioRxiv, https://doi.org/10.1101/2022.08.31.505989 https://doi.org/10.1101/2022.08.31.505989.
107. Ghosh, S., Körte, A., Serafini, G., Yadav, V., and Rodenfels, J. (2023). Developmental energetics: Energy expenditure, budgets and metabolism during animal embryogenesis. Seminars in Cell & Developmental Biology *138*, 83–93. https://doi.org/10.1016/j.semcdb.2022.03.009.
108. Gillette, C.M., Tennessen, J.M., and Reis, T. (2021). Balancing Energy Expenditure and Storage with Growth and Biosynthesis during Drosophila Development. Dev Biol *475*, 234–244. https://doi.org/10.1016/j.ydbio.2021.01.019.
109. Jemielita, M., Taormina, M.J., Burns, A.R., Hampton, J.S., Rolig, A.S., Guillemin, K., and Parthasarathy, R. (2014). Spatial and Temporal Features of the Growth of a Bacterial Species Colonizing the Zebrafish Gut. mBio *5*, 10.1128/mbio.01751-14. https://doi.org/10.1128/mbio.01751-14.
110. McKenney, E.A., Hale, A.R., Anderson, J., Larsen, R., Grant, C., and Dunn, R.R. (2023). Hidden diversity: comparative functional morphology of humans and other species. PeerJ *11*, e15148. https://doi.org/10.7717/peerj.15148.
111. Ventura, A.K., and Mennella, J.A. (2017). An Experimental Approach to Study Individual Differences in Infants' Intake and Satiation Behaviors during Bottle-Feeding. Child Obes *13*, 44–52. https://doi.org/10.1089/chi.2016.0122.
112. Flores, E.M., Nguyen, A.T., Odem, M.A., Eisenhoffer, G.T., and Krachler, A.M. (2020). The Zebrafish as a Model for Gastrointestinal Tract - Microbe Interactions. Cellular microbiology *22*, e13152. https://doi.org/10.1111/cmi.13152.
113. Sant, K.E., and Timme-Laragy, A.R. (2018). Zebrafish as a Model for Toxicological Perturbation of Yolk and Nutrition in the Early Embryo. Curr Environ Health Rep *5*, 125–133. https://doi.org/10.1007/s40572-018-0183-2.
114. White, R.M., Sessa, A., Burke, C., Bowman, T., LeBlanc, J., Ceol, C., Bourque, C., Dovey, M., Goessling, W., Burns, C.E., et al. (2008). Transparent Adult Zebrafish as a Tool for In Vivo Transplantation Analysis. Cell Stem Cell *2*, 183–189. https://doi.org/10.1016/j.stem.2007.11.002.

115. McGraw, H.F., Snelson, C.D., Prendergast, A., Suli, A., and Raible, D.W. (2012). Postembryonic neuronal addition in Zebrafish dorsal root ganglia is regulated by Notch signaling. Neural Dev *7*, 23. https://doi.org/10.1186/1749-8104-7-23.
116. Abramsson, A., Kettunen, P., Banote, R.K., Lott, E., Li, M., Arner, A., and Zetterberg, H. (2013). The zebrafish amyloid precursor protein-b is required for motor neuron guidance and synapse formation. Developmental Biology *381*, 377–388. https://doi.org/10.1016/j.ydbio.2013.06.026.
117. Barr, Y., and Helland, S. (2007). A Simple Method for Mass-Production of Liposomes, in Particular Large Liposomes, Suitable for Delivery of Free Amino Acids to Filter Feeding Zooplankton. Journal of Liposome Research *17*, 79–88. https://doi.org/10.1080/08982100701375050.
118. Schaefer, M.A., Nelson, H.N., Butrum, J.L., Gronseth, J.R., and Hines, J.H. (2023). A low-cost smartphone fluorescence microscope for research, life science education, and STEM outreach. Sci Rep *13*, 2722. https://doi.org/10.1038/s41598-023-29182-y.
119. Oesterle, A. (2018). Pipette Cookbook.
120. Giovannucci, A., Friedrich, J., Gunn, P., Kalfon, J., Brown, B.L., Koay, S.A., Taxidis, J., Najafi, F., Gauthier, J.L., Zhou, P., et al. (2019). CaImAn an open source tool for scalable calcium imaging data analysis. eLife *8*, e38173. https://doi.org/10.7554/eLife.38173.
121. Pnevmatikakis, E.A., and Giovannucci, A. (2017). NoRMCorre: An online algorithm for piecewise rigid motion correction of calcium imaging data. J. Neurosci. Methods *291*, 83–94. https://doi.org/10.1016/j.jneumeth.2017.07.031.
122. Pnevmatikakis, E.A., Soudry, D., Gao, Y., Machado, T.A., Merel, J., Pfau, D., Reardon, T., Mu, Y., Lacefield, C., Yang, W., et al. (2016). Simultaneous Denoising, Deconvolution, and Demixing of Calcium Imaging Data. Neuron *89*, 285–299. https://doi.org/10.1016/j.neuron.2015.11.037.
123. Beare, R., Lowekamp, B., and Yaniv, Z. (2018). Image Segmentation, Registration and Characterization in R with SimpleITK. Journal of Statistical Software *86*, 1–35. https://doi.org/10.18637/jss.v086.i08.
124. Yaniv, Z., Lowekamp, B.C., Johnson, H.J., and Beare, R. (2018). SimpleITK Image-Analysis Notebooks: a Collaborative Environment for Education and Reproducible Research. J Digit Imaging *31*, 290–303. https://doi.org/10.1007/s10278-017-0037-8.
125. Lowekamp, B.C., Chen, D.T., Ibanez, L., and Blezek, D. (2013). The Design of SimpleITK. Front. Neuroinform. *7*. https://doi.org/10.3389/fninf.2013.00045.
126. Smithson, M., and Verkuilen, J. (2006). A better lemon squeezer? Maximum-likelihood regression with beta-distributed dependent variables. Psychol Methods *11*, 54–71. https://doi.org/10.1037/1082-989X.11.1.54.

A Complex particles (CPs) for odorless feeding

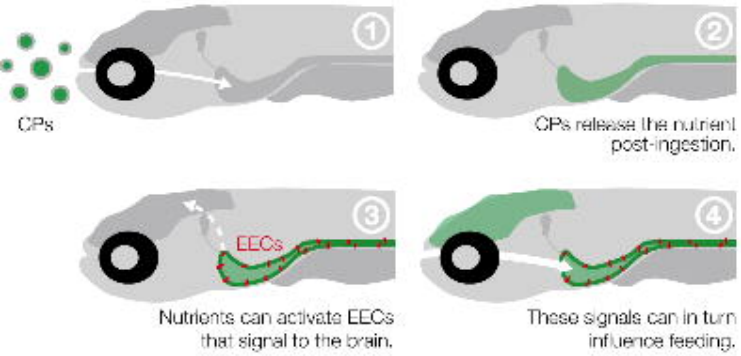

B

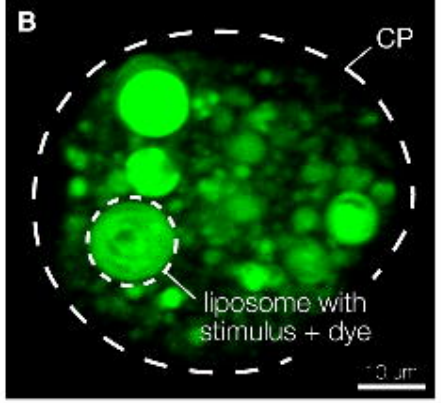

C Gut-mediated feeding assay

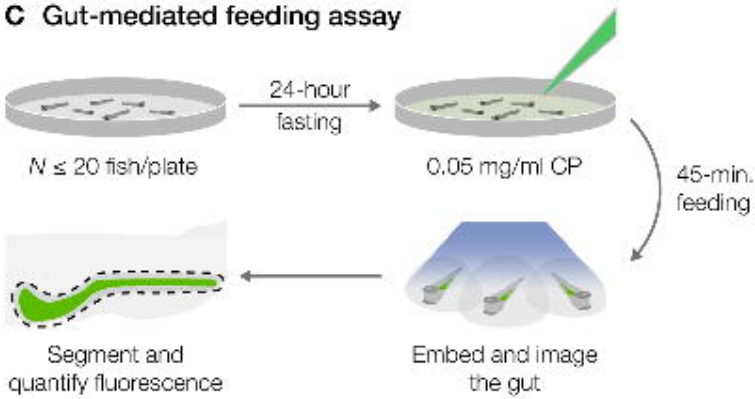

D Tested particles

Empty (Ctrl)	*Contains only the fluorescent dye. Control for batch differences.*
NaCl	*Aversive to zebrafish. Control for olfactory detection and avoidance.* (Lovett-Barron et al., 2020; Herrera et al., 2021)
Glucose (Glu)	*Activates zebrafish EECs. Known to be rewarding in mammals.* (Ye et al., 2019; Ren et al., 2010)
Glycine (Gly)	*Associated with prey, and stimulates feeding in fish.* (Webb and Johannes, 1967; Carr et al., 1996)
Alanine (Ala)	*Associated with prey, and stimulates feeding in fish.* (Webb and Johannes, 1967; Carr et al., 1996)

E

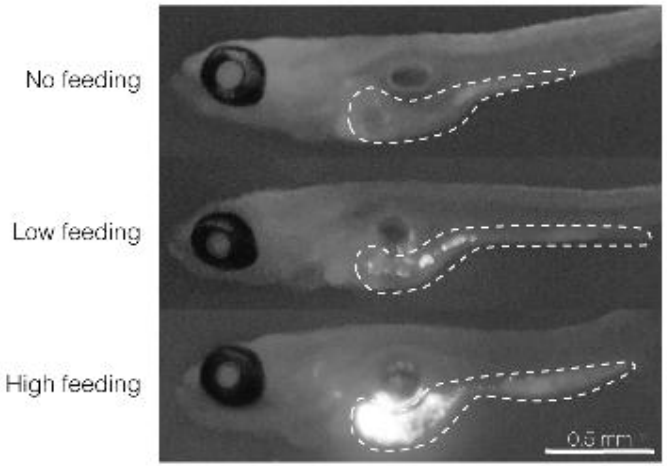

F Gly and Ala in the gut increases feeding

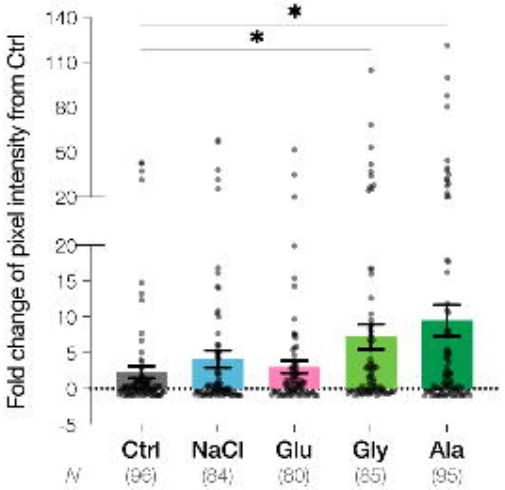

G Chemogenetic ablation of EECs (EEC^{DTA})

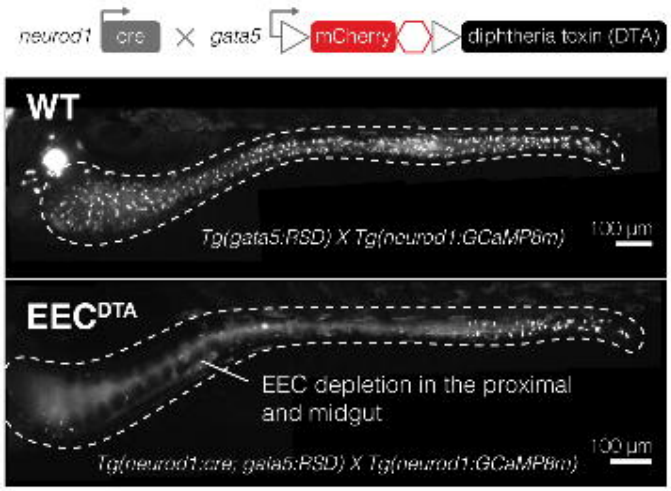

H EEC^{DTA} fish have altered food approach behavior

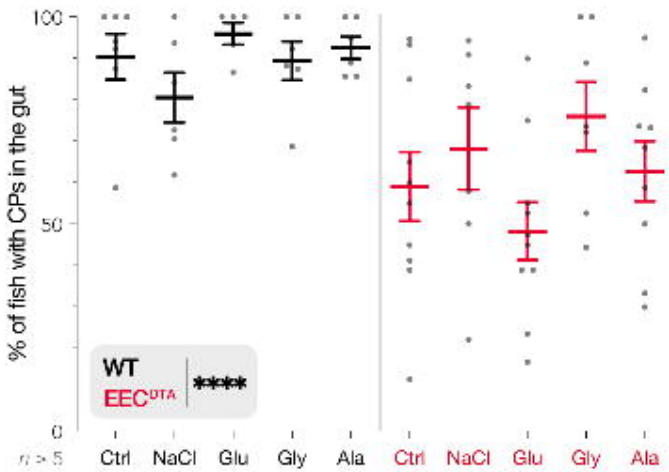

I EEC^{DTA} fish increase nutrient feeding

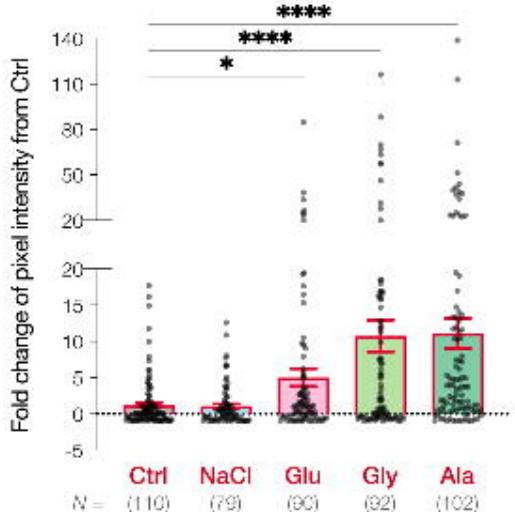

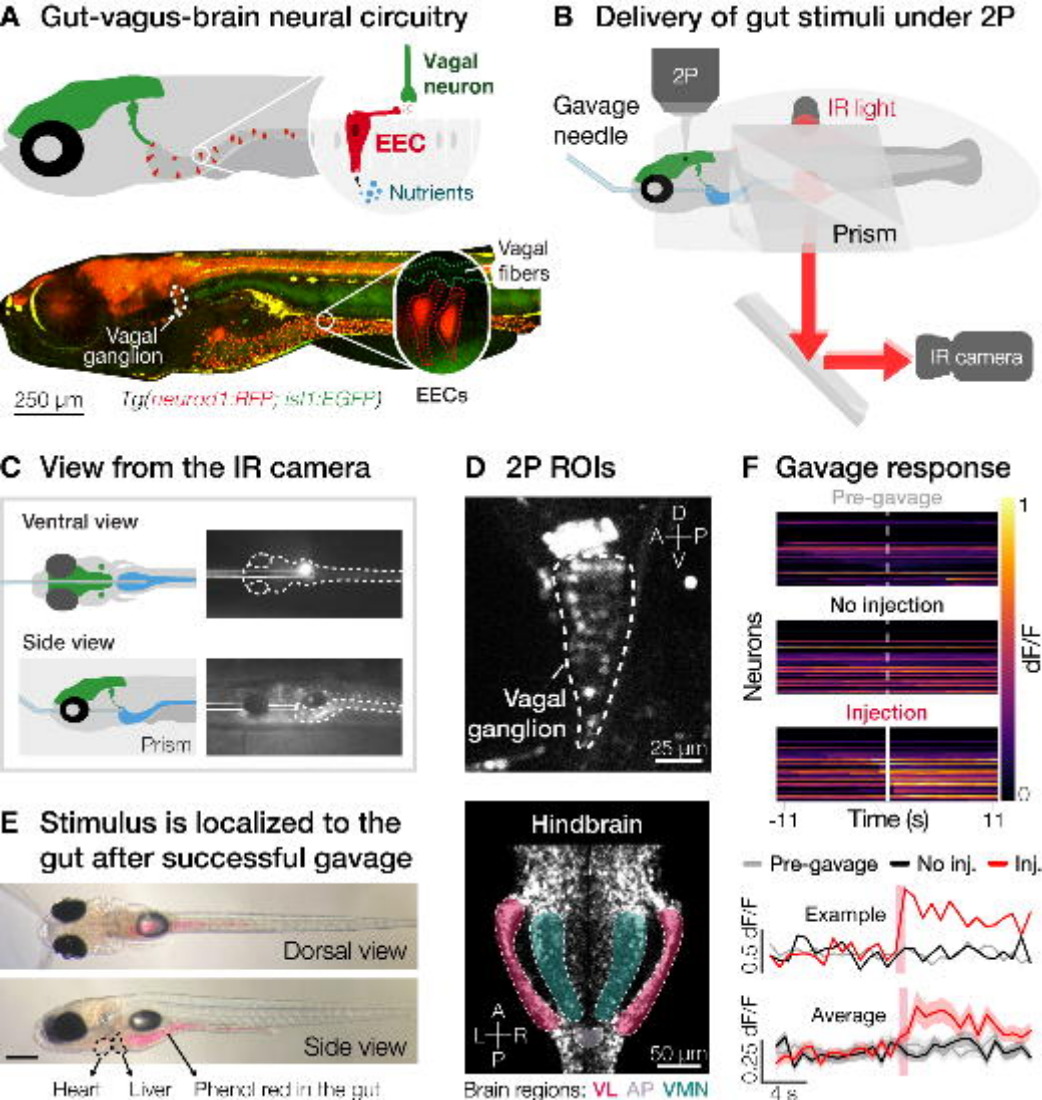
A Gut-vagus-brain neural circuitry
Vagal neuron
EEC
Nutrients
Vagal fibers
Vagal ganglion
250 µm
Tg(neurod1:RFP; isl1:EGFP)
EECs
B Delivery of gut stimuli under 2P
2P
Gavage needle
IR light
Prism
IR camera
C View from the IR camera
Ventral view
Side view
Prism
D 2P ROIs
D
A
P
V
Vagal ganglion
25 µm
Hindbrain
A
L
R
P
50 µm
Brain regions: VL AP VMN
E Stimulus is localized to the gut after successful gavage
Dorsal view
Side view
Heart
Liver
Phenol red in the gut
F Gavage response
Pre-gavage
No injection
Injection
Neurons
dF/F
1
0
-11
Time (s)
11
Pre-gavage
No inj.
Inj.
Example
0.5 dF/F
Average
0.25 dF/F
4 s

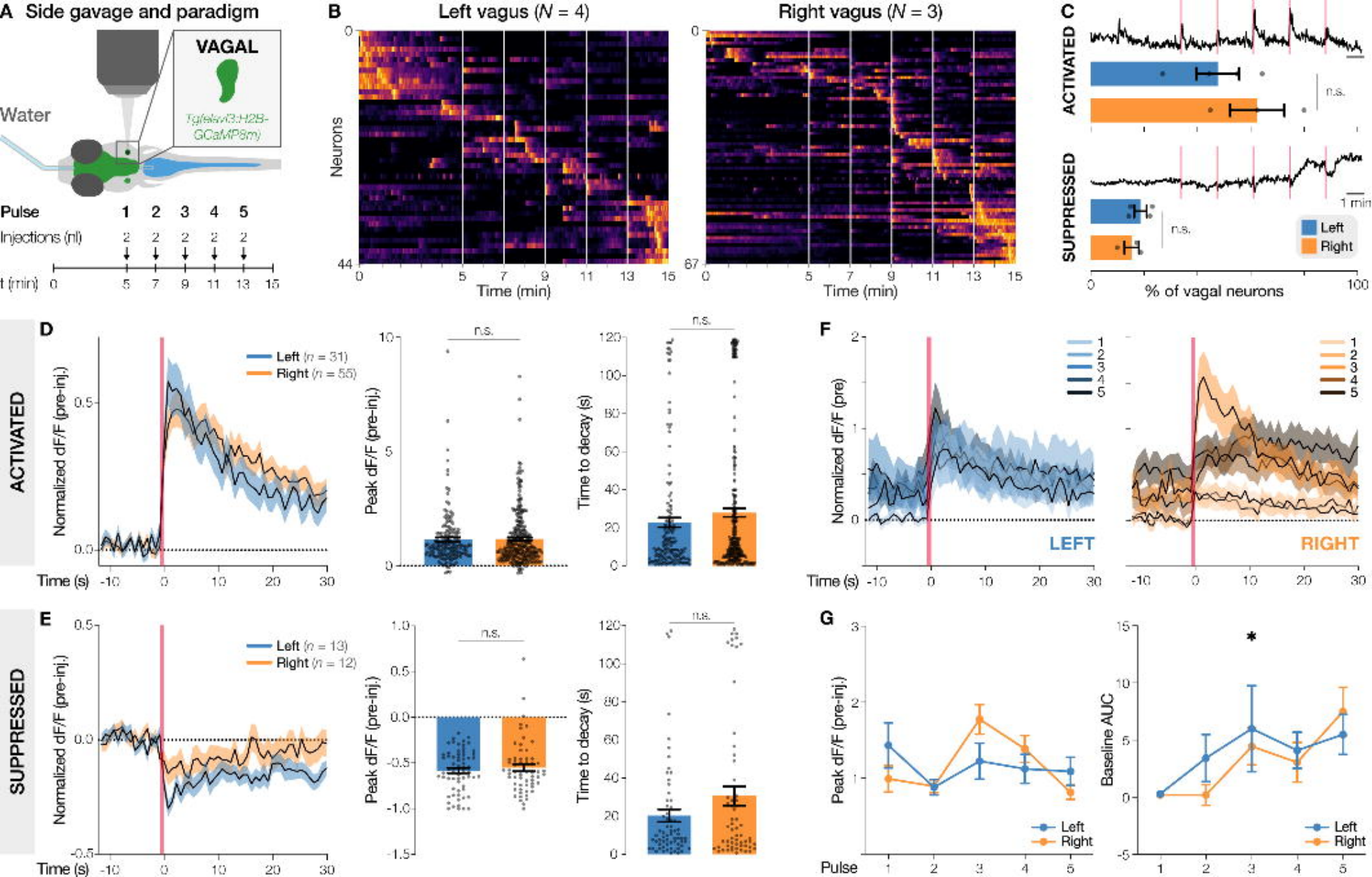
A Side gavage and paradigm
VAGAL
Tg(elavl3:H2B-GCaMP8m)
Water
Pulse 1 2 3 4 5
Injections (nl) 2 2 2 2 2
t (min) 0 5 7 9 11 13 15
B
Left vagus (N = 4)
Right vagus (N = 3)
Neurons
Time (min)
C
ACTIVATED
SUPPRESSED
n.s.
1 min
Left
Right
% of vagal neurons
D
ACTIVATED
Left (n = 31)
Right (n = 55)
Normalized dF/F (pre-inj.)
Peak dF/F (pre-inj.)
Time to decay (s)
Time (s)
E
SUPPRESSED
Left (n = 13)
Right (n = 12)
F
Normalized dF/F (pre)
LEFT
RIGHT
G
Peak dF/F (pre-inj.)
Baseline AUC
Pulse

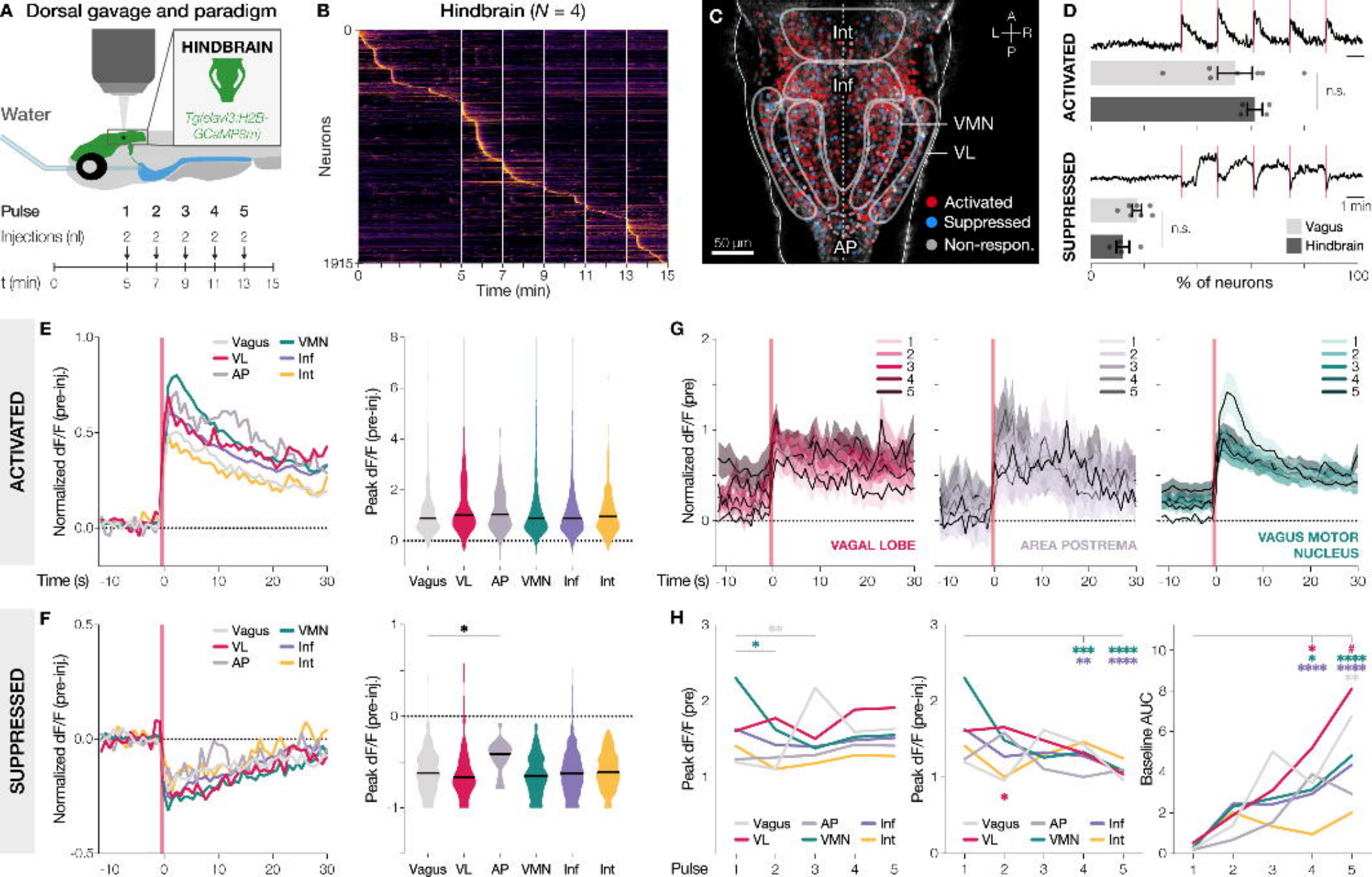
A Dorsal gavage and paradigm
HINDBRAIN
Tg(elavl3:H2B-GCaMP8m)
Water
Pulse 1 2 3 4 5
Injections (nl) 2 2 2 2 2
t (min) 0 5 7 9 11 13 15
B Hindbrain (N = 4)
Neurons
Time (min)
C
Int
Inf
VMN
VL
AP
A
L R
P
50 µm
Activated
Suppressed
Non-respon.
D
ACTIVATED
SUPPRESSED
n.s.
1 min
Vagus
Hindbrain
% of neurons
E
ACTIVATED
Vagus VMN VL Inf AP Int
Normalized dF/F (pre-inj.)
Peak dF/F (pre-inj.)
Time (s)
Vagus VL AP VMN Inf Int
G
Normalized dF/F (pre)
VAGAL LOBE
AREA POSTREMA
VAGUS MOTOR NUCLEUS
Time (s)
F
SUPPRESSED
Normalized dF/F (pre-inj.)
Peak dF/F (pre-inj.)
H
Peak dF/F (pre)
Peak dF/F (pre-inj.)
Baseline AUC
Vagus AP Inf VL VMN Int
Pulse

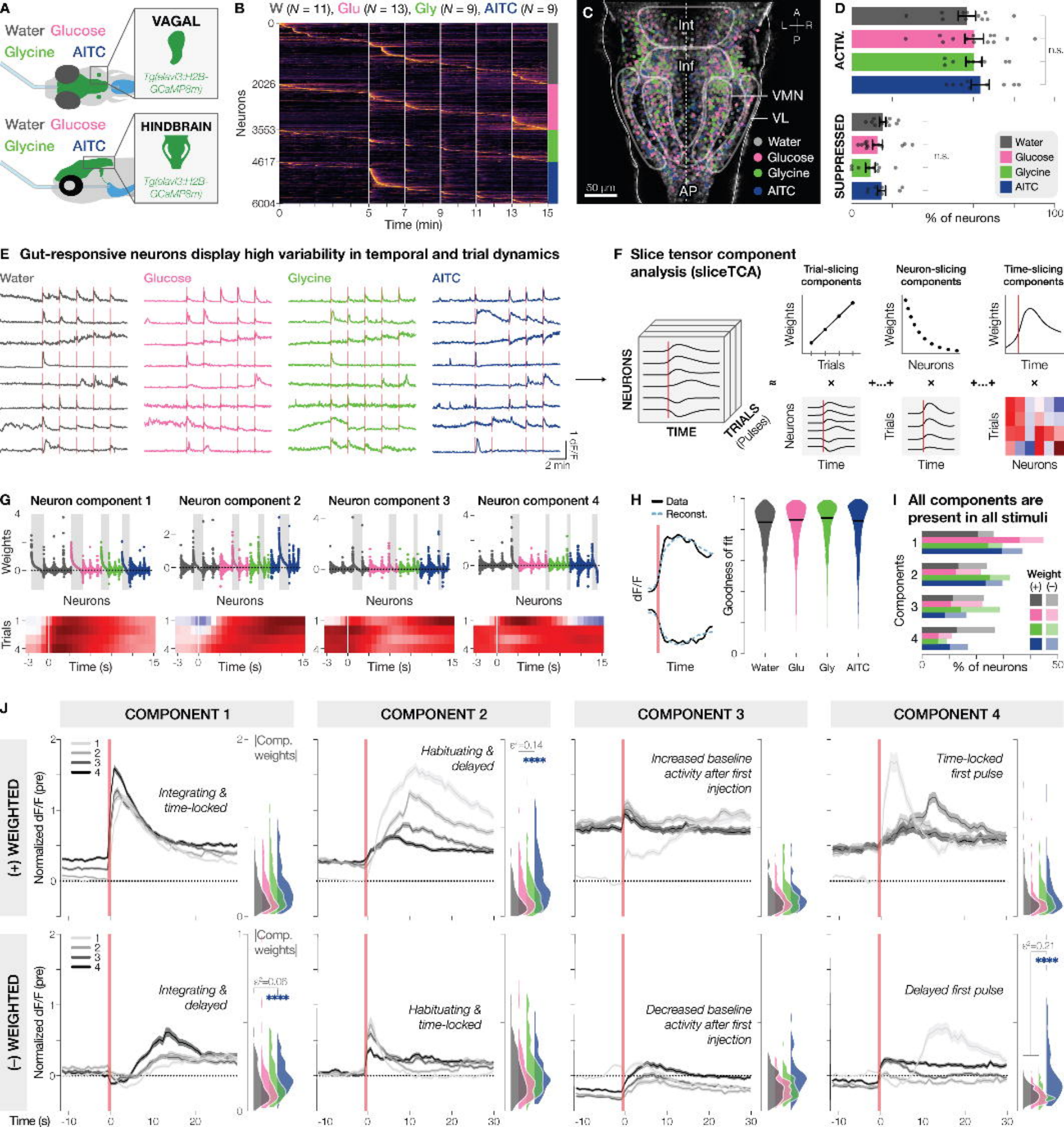
A
Water Glucose
Glycine AITC
VAGAL
Tg(elavl3:H2B-GCaMP8m)
Water Glucose
Glycine AITC
HINDBRAIN
Tg(elavl3:H2B-GCaMP8m)
B
W (N = 11), Glu (N = 13), Gly (N = 9), AITC (N = 9)
Neurons
Time (min)
C
Int
Inf
VMN
VL
AP
50 µm
Water
Glucose
Glycine
AITC
D
ACTIV.
SUPPRESSED
n.s.
% of neurons
E Gut-responsive neurons display high variability in temporal and trial dynamics
Water
Glucose
Glycine
AITC
1 dF/F
2 min
F Slice tensor component analysis (sliceTCA)
NEURONS
TIME
TRIALS (Pulses)
Trial-slicing components
Neuron-slicing components
Time-slicing components
Weights
Trials
Neurons
Time
G
Neuron component 1
Neuron component 2
Neuron component 3
Neuron component 4
Weights
Neurons
Trials
Time (s)
H
Data
Reconst.
dF/F
Time
Goodness of fit
Water
Glu
Gly
AITC
I All components are present in all stimuli
Components
Weight
(+) (−)
% of neurons
J
COMPONENT 1
COMPONENT 2
COMPONENT 3
COMPONENT 4
(+) WEIGHTED
(−) WEIGHTED
Normalized dF/F (pre)
|Comp. weights|
Integrating & time-locked
Habituating & delayed
Increased baseline activity after first injection
Time-locked first pulse
Integrating & delayed
Habituating & time-locked
Decreased baseline activity after first injection
Delayed first pulse
Time (s)

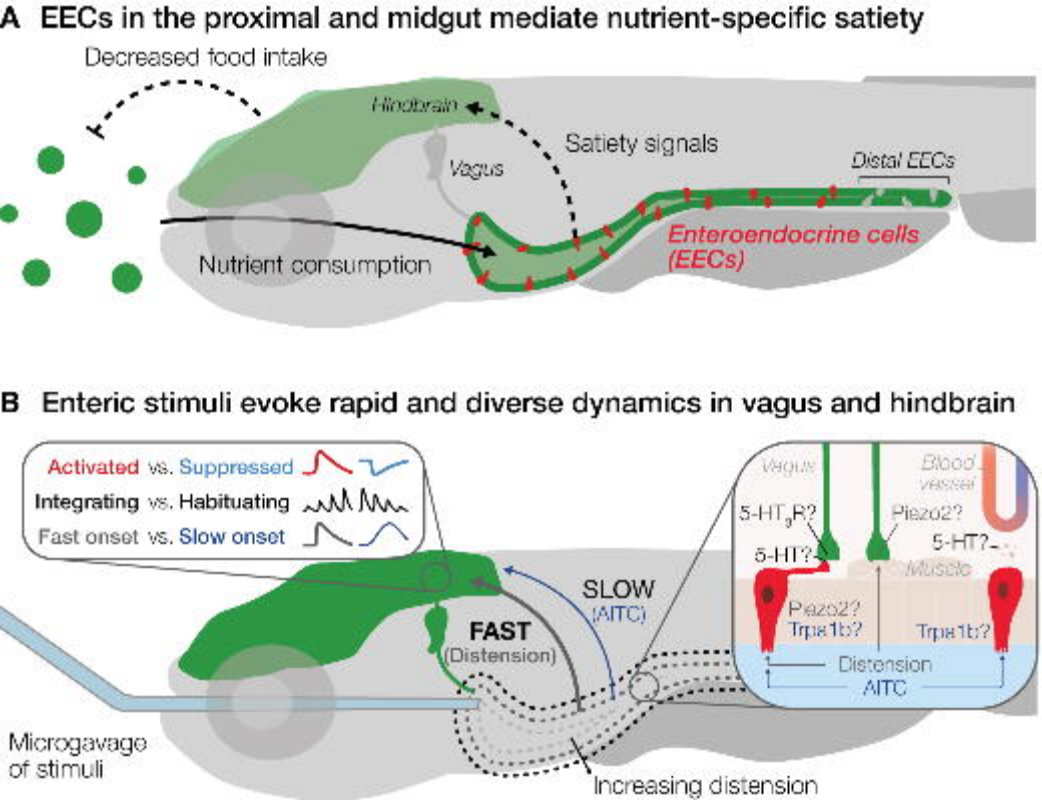
A EECs in the proximal and midgut mediate nutrient-specific satiety
Decreased food intake
Hindbrain
Satiety signals
Vagus
Distal EECs
Enteroendocrine cells
(EECs)
Nutrient consumption
B Enteric stimuli evoke rapid and diverse dynamics in vagus and hindbrain
Activated vs. Suppressed
Integrating vs. Habituating
Fast onset vs. Slow onset
SLOW
(AITC)
FAST
(Distension)
Microgavage
of stimuli
Increasing distension
Vagus
Blood
vessel
5-HT3R?
Piezo2?
5-HT?
5-HT?
Muscle
Piezo2?
Trpa1b?
Trpa1b?
Distension
AITC